

Symmetry breaking and period doubling on a torus in the VLF regime in Taylor-Couette flow

J. von Stamm,¹ U. Gerdts,¹ Th. Buzug,² and G. Pfister^{1,*}

¹*Institut für Angewandte Physik, Universität Kiel, Olshausenstraße 40, D-24098 Kiel, Germany*

²*Philips Research, Technical Systems Hamburg, Röntgenstrasse 24-26, D-22315 Hamburg, Germany*

(Received 28 February 1996)

We present an extensive experimental study of the very-low-frequency (VLF) mode, a very slow time-periodic oscillation with azimuthal wave number $m=0$ in axisymmetric Taylor-Couette flow. The VLF mode appears as a secondary or higher time-dependent instability in the entire wavelength range for flow systems with radius ratio 0.5. We focus on measurements which cover a parameter range that reaches from the onset of time dependence to the transition to chaos in the wavelength range $\lambda < 1.78d$ (d is the gap width of the cylinder) appearing in flow systems having 10–50 vortices. It was found that, increasing the Reynolds number, one observes—independently of the number of vortices of the flow system—always the same “sequence” of states. This is, first, the transition from Taylor vortex flow to the onset of the time-periodic small-jet mode via a Hopf bifurcation going along with a simultaneous breaking of the axial symmetry of the flow, second, the onset of the VLF mode via a homoclinic bifurcation for smaller cylinders where the underlying wavy Taylor vortex flow is still the small-jet mode (therefore we have a T^2 torus); and finally, the transitions to chaos, which were found to occur as period-doubling routes on T^2 tori. Additionally a quantitative description of this transition to chaos is given, calculating the correlation dimension on the basis of a proper reconstructed phase space. A model of interacting time-dependent Taylor vortex flow is discussed and compared to the appearance of VLF-mode oscillations in the flow. [S1063-651X(96)08410-3]

PACS number(s): 47.20.-k, 05.45.+b

I. INTRODUCTION

The Taylor-Couette flow reported here consists of a viscous fluid between two concentric cylinders with the inner one rotating, while the outer cylinder and end plates are held at rest. When the Reynolds number Re is very small, the flow appears to be a circular shear flow, the *circular Couette flow* (CCF). The end plates cause only small perturbations on this flow when the cylinder is long enough, but they have a crucial effect on the bifurcations obtained for the infinite cylinder model. However, when Re is increased to a quasicritical range near Re_{TVF} , the flow becomes centrifugally unstable and changes to a regular cellular vortex structure in which ring vortices alternating in flow direction enclose the axis of rotation. The flow remains stationary and the vortex structure is axisymmetric and periodic in the axial direction with wavelength λ . This flow is called *Taylor vortex flow* (TVF) after Taylor [1], who first described it experimentally and theoretically. In an experiment one has a system with finite ends, following that the transition to TVF takes place as a disconnected pitchfork bifurcation where the vortices grow in smoothly from the ends. This boundary-induced effect causes a disconnection by a factor of approximately 2.5, i.e., the ratio of the critical Reynolds numbers of the anomalous and the normal TVF modes [2–4], only the latter we consider here.

Increasing the inner cylinder's angular velocity Ω_1 , which is proportional to the Reynolds number, the flow undergoes a series of transitions (the “main sequence”) which are characterized by changes in the symmetry group that leaves the flow invariant [5]. The Navier-Stokes equations linearized

around Taylor vortex flow are autonomous in Θ and t , so generically any mode which breaks these symmetries will have the mathematical form of a rotating wave. In this time-dependent flow regime, which is referred to as *wavy Taylor vortex flow* (WVF), the motion becomes time independent when observed in a corotating frame [6]. Transitions to WVF have been observed experimentally by Coles in his seminal paper [7], and different aspects of WVF by King and Swinney [8], King [9], Pfister *et al.* [10,11] and Park [12]. The sensitive dependence of the critical Reynolds number of the first Hopf bifurcation on the number of cells in a given cylinder length was investigated by Mullin and Benjamin [13] and Mullin [14] first and later studied in detail by Gerdts *et al.* [15]. Numerical studies have been performed by Davey *et al.* [16], Jones [17], Marcus [18], Edwards *et al.* [19] and DiPrima *et al.* [20], for example. Depending on the geometrical boundary conditions there can exist different wavy Taylor vortex flows, amongst them the “classical” Wavy mode [15,17]. To exclude misunderstandings concerning the labeling of the “Wavy mode” and the “wavy Taylor vortex flow” we often refer to the latter as “time-periodic (Taylor vortex) flow.”

At larger Reynolds numbers the azimuthally traveling wave can bifurcate to a doubly periodic flow regime, which is temporally periodic when viewed from the frame rotating at the wave speed of the underlying time-periodic flow mode. This transition may again be accompanied by a change in the azimuthal symmetry [21] and the appearing doubly periodic flow is called *modulated wavy vortex flow* (MWVF). Such flows have been investigated experimentally by Gorman and Swinney (GS mode) [22] and Zhang and Swinney (ZS mode) [23], occurring as preturbulent flow regimes [24,25], by King and Swinney (KS mode) [8] occurring as a result of the competition of at least two WVF

*Electronic address: pfister@ang-physik.uni-kiel.de

modes for dominance. Mullin *et al.* [26] found that, decreasing the Reynolds number, the interaction between a symmetry-breaking bifurcation and a fold point gives rise to subcritical Hopf bifurcation points to a tilt wave (an axially localized azimuthally traveling wave with azimuthal wave number $m=1$) and the onset of a modulation of this tilt wave. Additionally they experimentally and numerically discovered an $m=0$ mode which is then modulated at a secondary Hopf bifurcation by an $m=1$ mode.

In an extensive numerical study of MWVF, Coughlin and Marcus have performed numerical simulations of the stability of GS and ZS modes, showing that several branches of quasiperiodic solutions exist, and not all of them occur as direct bifurcations from rotating waves as the main sequence suggests [21]. Furthermore the modulated flows studied in [8] and [26] and the appearance of the axisymmetric VLF mode as a secondary time-dependent flow [15] show that the main sequence does not seem to display a universal behavior in Taylor-Couette flow where the outer cylinder is held at rest. In fact, it is doubtful that the work of Golubitzky and Stewart [5] is directly relevant to flows where the outer cylinder is at rest, because, first, in this case modulation occurs at a value of Re several times larger than the critical value for the time-periodic flow; second, Golubitzky and Stewart looked at transitions in counterrotating cylinders (just) near a fixed ratio of the outer to inner cylinder rotation frequency for which six eigenmodes of CCF become unstable at the same inner cylinder rotation frequency [27]; and, third, the flows with radius ratio $\eta < 0.77$ show qualitatively different behavior compared to the flows with radius ratio $\eta > 0.79$, i.e., for narrow gaps, the transition to WVF takes place at a low value of Re near $1.2 \text{ Re}_{\text{TVF}}$, for wide gaps the onset of the waves is delayed to much higher Reynolds numbers [12,17,28,29]. Considering these facts we conclude that the main sequence, which is defined as the sequence of states

$$\text{CCF} \rightarrow \text{TVF} \rightarrow \text{WVF} \rightarrow \text{MWVF} \rightarrow \text{chaos},$$

is just useful as a schematic guide to the transitions in the system.

Here we are going to display an experimental study of a different main sequence to chaos in Taylor-Couette flow, which is valid for wide parameter ranges and thus may display a ‘‘general’’ behavior in this flow, at least for flow systems with radius ratio $\eta=0.5$. This is the sequence

$$\text{CCF} \rightarrow \text{TVF} \rightarrow \text{WVF} \rightarrow \text{VLF} \rightarrow \text{chaos}.$$

In the concluding section we also discuss this sequence of states in the context of a model of interacting time-dependent Taylor vortex flow developed by L’vov and Predtechensky [30–32]. In Sec. II we present the experimental setup of our flow system; in Sec. III, the measurement technique is discussed, which is necessary due to the different notations we use as a measure when the VLF mode appears. In the fourth section previous results on the VLF mode are presented to set our current results in context. In the next section a complete scenario in the 10-vortex flow for $\Gamma=8$ is presented to reveal the complexity of VLF mode. After that the symmetry breaking in large aspect ratio systems is investigated from $\Gamma=8$ up to $\Gamma=42$ (i.e., 10–50 vortices). This leads to the characterization of the bifurcation towards the VLF mode.

The VLF mode, together with the small-jet mode, exhibits period-doubling routes on tori to chaos which are investigated in the sixth section. Before the results are discussed in the final section, a quantitative characterization of this transition to chaos is presented in Sec. VII.

II. EXPERIMENTAL SETUP

The flow of interest is bounded by two high-precision coaxial cylinders. The rotating inner cylinder of the Taylor-Couette experiment is machined from stainless steel having a radius of $r_i=12.5$ mm. The stationary outer cylinder is made of optical polished glass with a radius of $r_o=25.0$ mm, giving a radius ratio of $\eta=0.5$. The accuracy of the radii is better than 0.01 mm over the entire length of 640 mm. We measured an eccentricity of the cylinders of $\varepsilon \leq 0.005$ mm and the power spectrum of the local velocity distribution is noticeable by the absence of Ω_i at any location in the fluid.

The top and bottom plates are at rest. The length of the gap can be varied continuously by moving the metal collar which provides the top surface of the flow domain. The aspect ratio $\Gamma=L/d$ used as a geometric control parameter is defined as the ratio of gap length L to gap width $d=r_o-r_i$. As a working fluid we use silicon oil with different viscosities ν depending on the flow situation. The Reynolds number is then defined as $\text{Re}=(\Omega_i r_i d)/\nu$. The temperature of the fluid is held constant to within 0.01 K by circulating thermostatically controlled oil through a surrounding square box. A phase locked loop (PLL) circuit controls the speed of the inner cylinder with an accuracy of better than one part in 10^{-4} in the short term and better than one part in 10^{-7} in the long-term average. The uncertainty of the absolute value of the Reynolds number is smaller than 1%.

The local velocity is measured by a real-fringe laser-Doppler velocimeter (LDV) and recorded by a PLL-analogue tracker. After filtering by an analog Bessel filter of fourth order, the velocity signal is fed into an analog-to-digital converter (ADC) with a 14-bit resolution and then into a computer where the data processing is performed. For more details of the experimental setup see [33].

III. MEASUREMENT TECHNIQUE

Presenting our experimental results we use different notations for the plots of the VLF-mode oscillations. The VLF mode has an azimuthal wave number $m=0$. This was confirmed by simultaneous measurements of the velocity in the time-dependent regime at different azimuthal angles having the same axial position. Therefore it can be understood as a very slow time-dependent shift of the whole bulk of time-periodic Taylor vortices with decaying shift amplitudes towards the ends. To make this clear and to represent the symmetry properties of the flow (in Sec. V) we used the *local* axial displacement Δz of the Taylor vortices instead of the axial velocity component $v_z(t)$ as a measure in the corresponding figures.

Indeed these two measures can be used identically and can be derived experimentally from each other by recording the axial velocity profile and determining the local gradient $\Delta z/\Delta v_z$ from this measurement. To detect the axial displacement of the vortices in most cases the best location for the

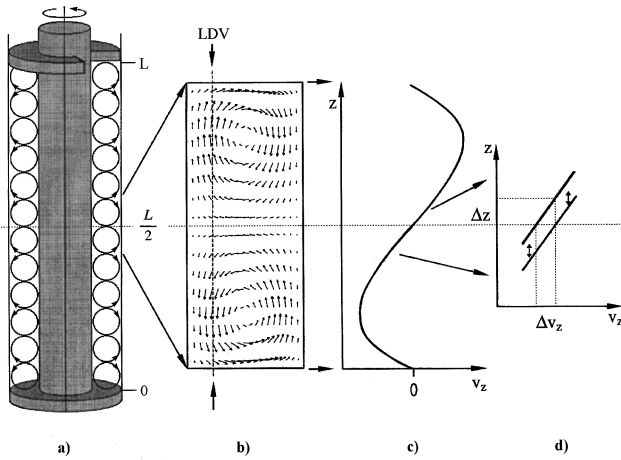


FIG. 1. (a) Taylor cylinder with schematically plotted flow field of a 12-vortex flow, (b) blowup of the flow field of two vortices in the middle of the cylinder, (c) the corresponding axial velocity component, recorded 3 mm from the inner cylinder [broken line in (b)], and (d) blowup of the local axial velocity component.

LDV measurement volume is the middle of the cylinder ($z = L/2$) in axial direction and a distance of $r = 2$ mm to $r = 3$ mm from the inner cylinder in radial direction. We demonstrate this in Figs. 1(a)–1(d). In Fig. 1(a) a Taylor cylinder with a schematically drawn 12-vortex flow and in Fig. 1(b) a blowup of the flow field of the two vortices in the middle is depicted. Figure 1(c) shows the corresponding velocity profile of the stationary flow field close to the onset of time dependence. It was recorded by moving the measurement volume continuously in axial direction with a distance of $r = 3$ mm from the inner cylinder. The axial trail of the LDV-measurement volume in the flow is marked with the broken vertical line in Fig. 1(b). Because the velocity profile is linear in this position ($z = L/2$) the changes in the axial velocity Δv_z are directly proportional to the axial displacement Δz of the vortex system [Fig. 1(d)]. Additionally to the oscillatory displacement caused by the VLF mode, the underlying vortex system can show an axial symmetry breaking. Therefore, when considering the symmetry properties of the flow system one has to determine the mean value of Δz . This yields the averaged axial displacement $\Delta \bar{z}$ as a measure for the axial symmetry of the flow.

IV. VLF MODE

In previous papers [15,34] we presented first results of the interaction of VLF-mode oscillations with different underlying WVF modes. To set our work in context, we present a brief review of these experimental findings.

The previous experimental investigations concentrated on smaller cylinders—especially the 10-vortex flow—covering the entire wavelength range of the underlying Taylor vortex flow. The VLF mode qualitatively and quantitatively differs from all other known time-periodic flows in the Taylor cylinder. In our experiments it always occurs as a secondary or higher time-dependent instability, whereby, it was shown that its occurrence depends on the strength of the spatial coupling of the oscillations of the underlying WVF modes. The fact, that the VLF mode appears in the entire wavelength

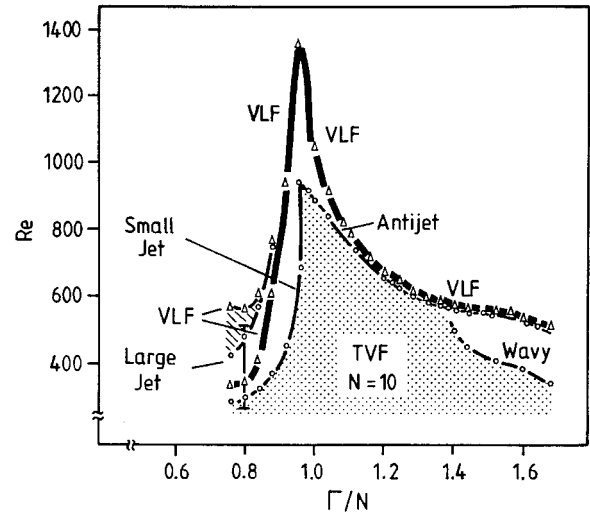


FIG. 2. Stability diagram for the onset of primary and higher time-dependent modes in the 10-vortex flow in a Taylor-Couette system with $\eta = 0.5$. The dotted section marks the stationary 10-vortex flow.

range as a secondary or higher time-dependent instability and that for increasing Reynolds numbers the flow in the VLF regime shows transitions to chaotic behavior, could be a hint to a universal significance of it.

The VLF mode appears in the entire range where the underlying Taylor vortices are stable, as shown in Fig. 2 for the 10-vortex flow. The onset of the VLF mode is marked with the thick lines including the triangles whereas all other measured stability lines in this diagram are marked with circles. Starting with stationary Taylor vortices (dotted section in Fig. 2), the lines denote the transitions to the time-periodic Taylor vortex regime when the Reynolds number is increased. In the experiments one observes physically different time-periodic Taylor vortex flows (WVF). The special physical type of these rotating waves depends on geometrical boundary conditions (compare to Fig. 1 and Table I in [15]). On the left-hand side the stability line for the onset of the small-jet mode is located, an oscillation of the outward flow while the inward flow remains stationary. Adjacent outward flows oscillate in antiphase. On the right-hand side the stability lines for the wavy mode, an axial oscillation of the entire vortex, and in midrange for the antijet mode, an oscillation having its main amplitude in the inward flow [15].

All experimental observations support the conjecture that there is a causal connection between the appearance of the VLF mode and the presence of the underlying time-periodic flow modes. The shift of the phases of oscillations in neighboring vortices causes the occurrence of the VLF mode which appears in the entire measured Γ range. The interaction of the VLF mode with the underlying time-periodic flow modes reveals that the VLF mode is caused by the strength of coupling of the phases of the underlying time-periodic flow modes. These modes cause a variation of the wavelength of the vortices in the flow. So there is a coupling between these modes and an axial phase diffusion. Furthermore the wave speeds of the time-periodic flow modes depend on the wavelength of the vortices. Due to this a local disturbance of the wavelength leads to a change in the wave

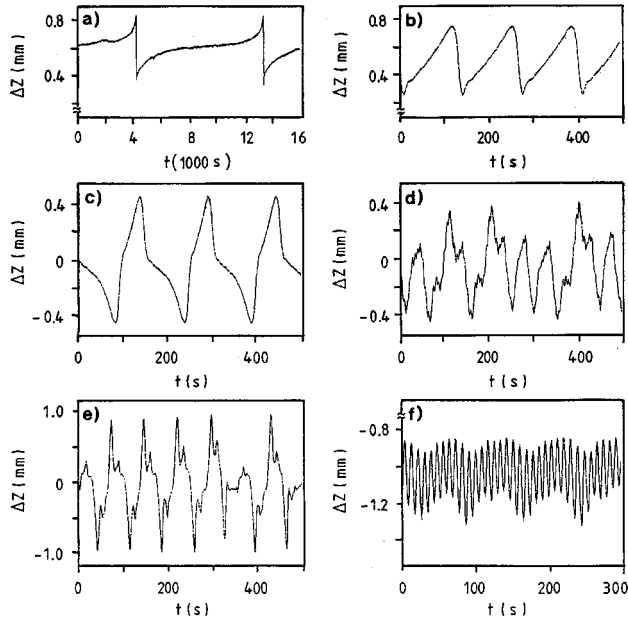


FIG. 3. Six different VLF oscillations recorded in the 10-vortex flow at $\Gamma=8$ ($\Gamma/N=0.80$). (a) for $Re=356.4$, (b) for $Re=365.4$, (c) for $Re=405.0$, (d) for $Re=454.3$, (e) for $Re=479.0$ and (f) for $Re=612.4$. Note the different time scales.

speed. A shift of the phases between the oscillations of neighboring vortices occurs. These phase differences are most likely the driving forces for the VLF mode.

The VLF mode shows various features and different dependence of amplitude A and frequency ω_{VLF} on Reynolds number Re , depending on the underlying time-dependent flows. In one example it occurs with a frequency starting from $\omega_{VLF}=0$ and a finite amplitude $A \neq 0$ when the underlying flow is a WVF, and on the other hand with a frequency having a finite value $\omega_{VLF} \neq 0$ and an amplitude increasing with a square-root law from the value $A=0$ corresponding to a Hopf bifurcation which was observed only when the underlying flow is a MWVF [15,35].

V. SYMMETRY BREAKING

To demonstrate, first, the large variety of VLF-mode oscillations, and second, the fact that the VLF mode not only appears in the entire wave-number range (as shown for the 10-vortex flow in Fig. 2) but also in wide Reynolds-number ranges, and thus influences the dynamics of the flow system in wide parameter ranges, we first of all give a view to a complete scenario for increasing Reynolds number, whereas, in the second part of this section, we focus on the symmetry breaking which appears simultaneously with the onset of the first time-dependent flow, the small-jet mode. This symmetry breaking leads to the onset of the VLF mode via a homoclinic bifurcation for smaller aspect ratios, which is shown in the last part of this section.

A. Complete scenario in the 10-vortex flow for $\Gamma=8$

Figures 3(a)–3(f), showing six different VLF oscillations for $\Gamma=8$ which are all recorded at $z=L/2$ in axial direction, reveals that some of the appearing VLF-mode oscillations

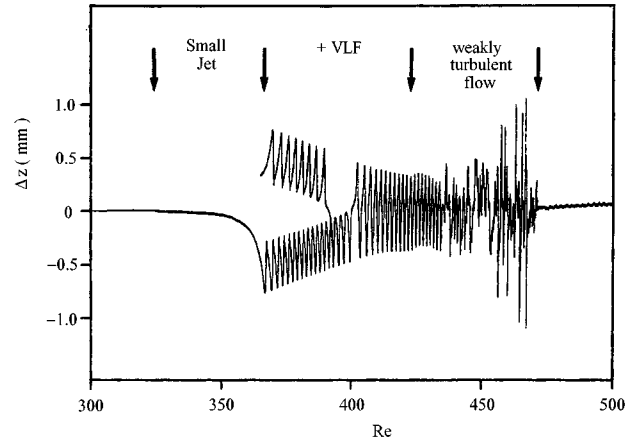


FIG. 4. Bifurcation diagram for the 10-vortex flow at $\Gamma=8$ ($\Gamma/N=0.80$). The axial displacement Δz is recorded versus the Reynolds number which is scanned from $Re=300$ to $Re=500$ with $\Delta Re/\Delta t=0.025 \text{ s}^{-1}$. The small-jet oscillations are averaged out to make the VLF-mode oscillations visible. The amplitude of the VLF mode can be depicted from the scan, while the oscillation gives only a qualitative impression of the frequency due to the measurement procedure.

are asymmetric in axial direction (breaking the $Z2$ symmetry). For all time-series depicted in the figure the local axial displacement Δz of the vortex pattern was recorded versus time t . Note the different, extremely long time scales. Due to symmetry arguments—neglecting imperfections due to the experimental setup—there always have to be VLF oscillations opposite in sign of Δz . This is shown in the bifurcation diagram in Fig. 4 for the 10-vortex flow for $\Gamma=8$, where the axial displacement Δz is recorded versus the Reynolds number which is scanned quasistatically from $Re=300$ to $Re=500$ with $\Delta Re/\Delta t=0.025 \text{ s}^{-1}$. The location of the LDV measurement was again placed in the midplane of the apparatus near the inner cylinder ($z=L/2$). Thus it is suitable to characterize deviations from the symmetric state where $\Delta z=0$. The vertical line in Fig. 2 marks the measurement route of the bifurcation diagram shown in Fig. 4. The plots of the bifurcation diagram in Fig. 4 and the time series in Fig. 3 are filtered with a low-pass Bessel filter of fourth order having a cutoff frequency at 0.1 Hz to make the structure of the VLF oscillation visible.

Considering the 10-vortex flow at $\Gamma=8$ one observes the onset of the small-jet mode at $Re_{SJ}=296.3$ and the onset of the VLF mode at $Re_{VLF}=356.4$. A delay of the critical Reynolds numbers in Fig. 4 is due to the quasistatic recording. As depicted in Fig. 5, where the frequency of the VLF mode is plotted versus Reynolds number, the frequency of the VLF oscillation goes to zero at onset (marked with triangles Δ in this figure). Figure 3(a) shows this oscillation slightly above its onset with a frequency of approximately $\omega_{VLF}=0.1 \text{ mHz}$ corresponding to a period of about 2.5 h. The vortex system needs almost the whole period to elongate into one end position while the elongation back to the opposite end position needs only about 15 sec.

Whereas the frequency goes to zero at onset of the VLF mode at Re_{VLF} , the amplitude A and axial asymmetry Δz exhibit finite values as apparent from Figs. 5(b) and 5(c). If the Reynolds number is changed to values slightly below or

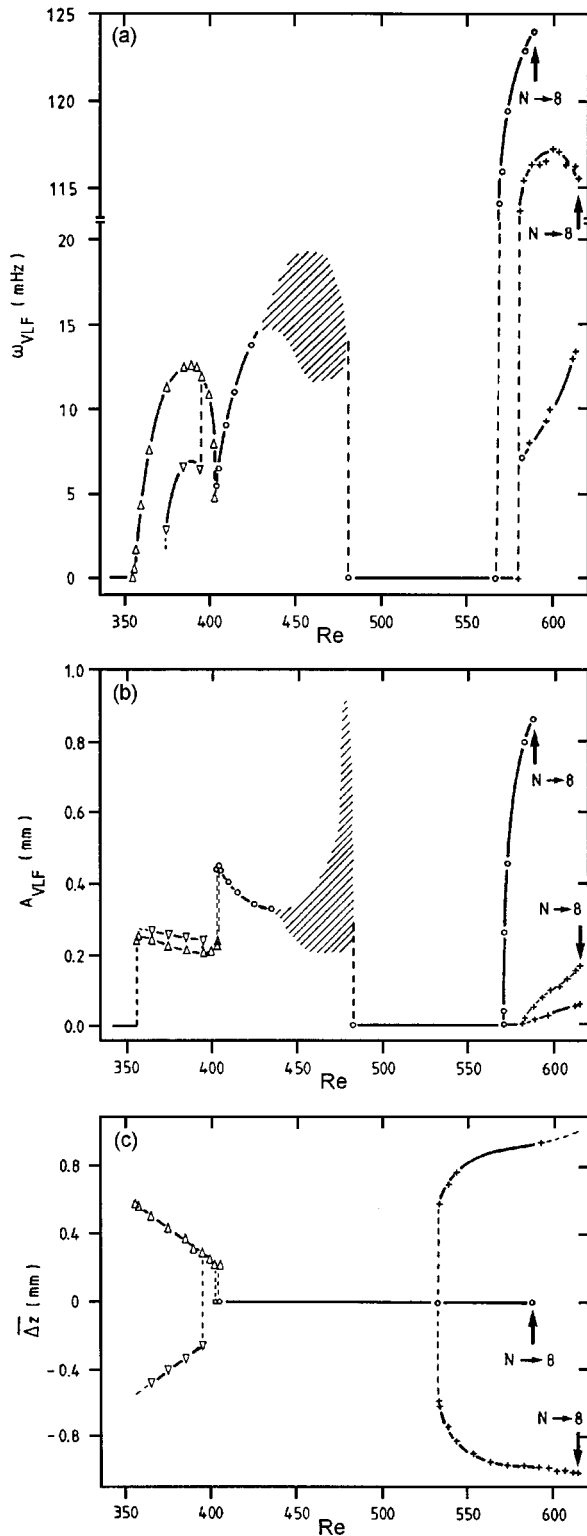


FIG. 5. (a) Frequency ω_{VLF} and (b) amplitude A_{VLF} of the VLF-mode oscillations plotted versus Reynolds number recorded in the 10-vortex flow for $\Gamma=8$ ($\Gamma/N=0.80$), (c) axial asymmetry Δz of the 10-vortex flow for $\Gamma=8$ ($\Gamma/N=0.80$) plotted versus Reynolds number.

above the onset of the VLF mode, no buildup or dying of the oscillation is observable. The oscillation appears with constant frequency ω_{VLF} and amplitude A and disappears immediately for Reynolds numbers $\text{Re} < \text{Re}_{\text{VLF}}$ showing an expo-

ponential decay of the temporary shift towards zero in opposite to the observations in WVF [11].

Increasing the Reynolds number the frequency ω_{VLF} grows rapidly [Fig. 5(a)] whereas amplitude A_{VLF} [Fig. 5(b)] and asymmetry Δz [Fig. 5(c)] show a slight fall off. A time series is shown in Fig. 3(b). Comparing Figs. 3(a) and 3(b) one realizes that the steep slope of the oscillation is nearly unaffected by a change in Reynolds number whereas, increasing the Reynolds number, the flat slope of the oscillation curve becomes more and more steep. In Fig. 3(a) the system needs about 9200 sec to reach the maximum shift whereas in Fig. 3(b) the period *only* lasts about 120 sec.

The VLF oscillations exhibiting values of Δz which are opposite in sign are marked with the symbols ∇ in the Fig. 5(a)–5(c). For $\Gamma=8$ this branch can be reached by a sudden jump in Reynolds number only. This is also apparent from Fig. 4 where the branch with positive Δz is disconnected. The frequencies of this state are approximately by a factor of 2 smaller whereas amplitude A_{VLF} [Fig. 5(b)] and axial asymmetry Δz [Fig. 5(c)] exhibit only little deviations from the values of the VLF flow appearing on the other branch. At $\text{Re}=395$ the flow state with positive Δz ends and the system jumps into the state with negative Δz [Fig. 4]. This reveals that the experimental apparatus has a small asymmetry which causes that one of the asymmetric branches is preferred. This has often been observed near bifurcation points (where the coercion forces are very small) and thus one branch is decoupled [36]. This apparative asymmetry can assume only very small extension, otherwise only one branch or even no VLF mode would be observable.

After the frequency ω_{VLF} of the VLF mode passes a maximum at $\text{Re} \approx 390$ it shows a strong decay for higher Reynolds numbers. At $\text{Re}=404$ a minimum is reached and one observes a sudden change in the structure of the VLF oscillation. A comparison of Figs. 3(b) with 3(c) reveals that the size of the amplitude becomes approximately twice as large as before [see Fig. 5(b), marked with circles \circ] and the asymmetry goes to zero, i.e., the flow becomes symmetric again [Fig. 5(c)]. This is also illustrated by the development of the VLF oscillation in the bifurcation diagram in Fig. 4. The transition between the symmetric and the asymmetric state exhibits a small hysteresis in Reynolds number. The branches are disconnected by an imperfection in the apparatus. But even assuming a perfect symmetry the VLF mode would not remain symmetric for decreasing Reynolds numbers and the symmetric branch does not coexist with both axially asymmetric branches, because it has to be an unstable solution of saddle-node type between $\text{Re}_{\text{VLF}}=356.4$ and $\text{Re}=404$. This is discussed in Sec. V C.

A further increase in the Reynolds number leads to a growth of the value of the frequency ω_{VLF} of the VLF mode, whereas its amplitude shows a slight decay [Figs. 5(a) and 5(b), symbols \circ], the flow remains symmetric in axial direction [Fig. 5(c)]. At $\text{Re} \approx 430$ the VLF oscillation becomes irregular in time and amplitude [marked with the hatched sections in Figs. 5(a) and (b)], i.e. the flow becomes weakly turbulent. Furthermore this chaotic flow is characterized by sudden jumps in phase of the VLF oscillation [Fig. 3(b)]; the flow still remains symmetric in axial direction [Fig. 5(c)]. Before the VLF mode disappears at $\text{Re}=482$ caused by the onset of the large-jet mode which shows a strong coupling of

the phases of neighbouring outward flows [15,37], the irregularities in frequency and amplitude pass a maximum. Fig. 3(e) reveals that after exceeding this maximum the chaotic flow shows a qualitative change. The irregularities in frequency and amplitude in the VLF oscillations have become small. When the system exceeds the critical value at $Re=482$ the amplitude of the VLF mode shows the form of a damped oscillation going towards zero. The Reynolds-number range between $Re=482$ and $Re=568.9$ is dominated by the appearance of the large-jet mode which, together with the small-jet mode, exhibits frequency locking which is in contradiction to previous theoretical considerations [37].

As apparent from Figs. 5(a)–5(c) the VLF mode shows a second onset at $Re=568.9$ exhibiting a quite different dependence of amplitude A and frequency ω_{VLF} on Reynolds number Re in this case. Other than at its first onset at $Re=356.4$ where it occurs with an frequency starting from $\omega_{VLF}=0$ and a finite amplitude $A \neq 0$, it here appears with an frequency having a finite value $\omega_{VLF} \neq 0$ and an amplitude increasing with a square-root law from the value $A=0$ corresponding to a Hopf bifurcation at second onset. The underlying flow modes are a time-periodic Taylor vortex flow in the first and a modulated wavy vortex flow in the second case [15], where the frequency of the VLF oscillation is approximately by a factor 10 larger than in the first case Fig. 5(a). The flow still remains axially symmetric [$\Delta z=0$, Fig. 5(c)].

A further smooth increase of the Reynolds number leads to a transition to 8-vortex flow at $Re=588.7$. Increasing the Reynolds number by a sudden change to $Re \approx 600$ the flow assumes two axially asymmetric states [marked with crosses (+) in Figs. 5(a)–5(c)]. As in the lower Reynolds-number range there are two corresponding asymmetric VLF-flow modes having opposite sign in Δz . The branch exhibiting positive Δz is preferred. This is again caused by the imperfection of the apparatus, but due to the coercion forces which are much larger compared to those in the lower Reynolds-number range, this asymmetry hardly influences the frequencies and amplitudes of both asymmetric branches.

Figure 3(f) reveals that the axially asymmetric VLF modes exhibits two superimposing oscillations. One observes a ‘‘high frequency’’ ($\omega_{VLF_1} \approx 120$ mHz) and a ‘‘slow frequency’’ component ($\omega_{VLF_2} \approx 10$ mHz). Both components of the VLF oscillation show an onset with amplitude $A=0$ and a finite value of frequency $\omega_{VLF_1}, \omega_{VLF_2} \neq 0$ at $Re=580.8$ [Figs. 5(a) and 5(b) marked with crosses (+)].

For Reynolds numbers $Re > 580.8$ the symmetric VLF mode also exhibits the slow frequency component ($\omega_{VLF_2} \approx 10$ mHz), but due to the fact that this branch becomes unstable against a transition to 8-vortex flow for lower Reynolds numbers, the amplitude of this oscillation remains small.

The axially asymmetric VLF modes remain stable towards larger Reynolds numbers than the symmetric flow state, exhibiting a transition to 8-vortex flow at $Re=615.3$. Towards smaller Reynolds numbers the asymmetric branches show a transition to the symmetric flow at $Re=532.4$ [Fig. 5(c)]. Due to the fact that the VLF oscillations disappear at $Re=580.8$, there exists a Reynolds-number range from $Re=532.4$ to $Re=580.8$ where both asymmetric

branches and the symmetric one coexist showing no VLF oscillation.

Comparing the bifurcation diagrams of the scenarios in Fig. 4, where $\Gamma/N=0.80$, and in Fig. 6 in [15], where the bifurcation diagram in 10-vortex flow for $\Gamma/N=0.84$ is shown, it is noticed that the flow in the smaller cylinder—slightly above the onset of the VLF mode—becomes symmetric again, whereas it remains axially asymmetric as long as the VLF mode is apparent, in larger aspect ratios. One observes that in smaller cylinders—up to the 8-vortex flow—the system exhibits no axial symmetry breaking simultaneously with the onset of the small-jet mode or prior to the onset of the VLF mode oscillation. In flow systems having more than 10 vortices there is always found an axial symmetry breaking going along with the onset of the small-jet mode (compare to the next section) and the flow always remains axially asymmetric as long as the VLF mode is apparent. The dynamical behavior in 10-vortex flow is different. Here both, the axially symmetric as well as the axially asymmetric states, depending on the wavelength of the Taylor vortices, occur in the limit of accuracy of the experiment.

B. Symmetry breaking in large aspect ratios

To study the axial symmetry breaking we concentrate on the analysis of the flow states in larger cylinders ($N \geq 10$) in the wavelength range $2\Gamma/N = \lambda < 1.78d$ where one observes—independently of the number N of the vortices of the flow system—always the same *sequence of states* appearing with increasing Reynolds number. This is, first, the transition from stationary TVF to the time-dependent small-jet mode via a Hopf bifurcation going along with a simultaneous breaking of the axial symmetry of the flow; second, the onset of the VLF mode via a homoclinic bifurcation for smaller cylinders where the underlying WVF is still the small-jet mode (therefore we have a T^2 torus) and finally, the transition to chaos (compare to Fig. 6 in [15] and to Fig. 4).

Due to the fact that the underlying WVF of the VLF mode is always the small-jet mode the VLF-flow states appearing in different aspect-ratio systems can be compared to each other and so this fact makes it possible to discover the dependence of this scenario on the geometrical boundary conditions, i.e., for increasing cylinder length. Such a comparison of flow states is not possible for $\lambda > 1.78d$, because in this wavelength range different WVF modes appear as first time-dependent instabilities showing different interactions with the underlying Taylor-vortex structure and the appearing VLF mode (compare to Fig. 1 in [15], examples for such different VLF modes are given in Fig. 3 in [15]).

It is remarkable that, simultaneously with the onset of the small-jet mode at the critical Reynolds number Re_{sj} , the flow undergoes an axial symmetry breaking, i.e., the Z_2 symmetry of the system is broken. This was measured for the 10-, 12-, 14-, 16-, 20-, 24-, 30-, 36-, 40-, 42-, 46-, and 50-vortex flow, and within an accuracy of ± 0.2 Reynolds numbers the symmetry breaking was observed to appear simultaneously with the onset of the time-dependent small-jet mode. Thus the flow bifurcates at Re_{sj} towards two branches which are symmetric to each other relative to the midplane of the cylinder. Figure 6 shows the profiles of the small-jet amplitude of both branches for the 30-vortex flow for different

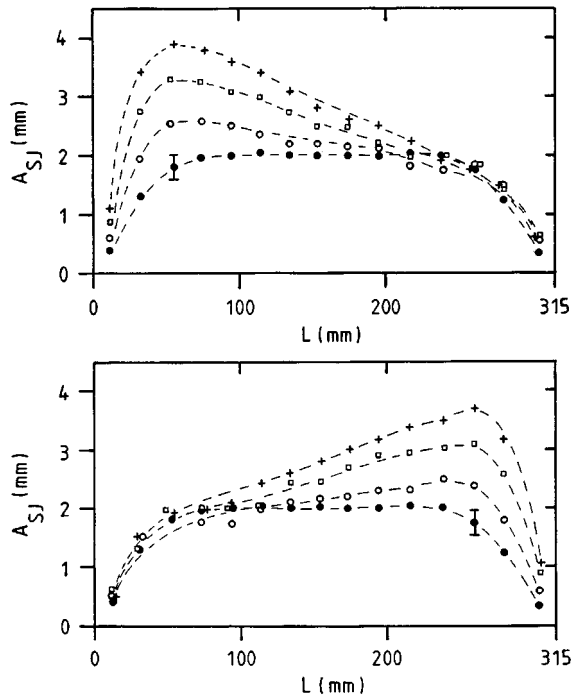


FIG. 6. Axial profiles of the small-jet amplitude of both branches recorded in 30-vortex flow for different Reynolds numbers at $\Gamma/N=0.84$, plotted versus axial position. The profile for $Re=361.7$ is marked with filled (\bullet) circles, for $Re=370.3$ is marked with open (\circ) circles, for $Re=377.2$ is marked with squares (\square), and for $Re=383.2$ is marked with crosses ($+$).

Reynolds numbers, reflecting this symmetry breaking. The profiles for $Re=361.7$ [marked with filled (\bullet) circles], $Re=370.3$ [marked with open (\circ) circles], $Re=377.2$ [marked with squares (\square)] and $Re=383.2$ [marked with crosses ($+$)] are plotted versus axial position, respectively. The axial position is given as the distance from the bottom plate in mm. Dimensionless units of the axial position can be obtained by dividing it by the gap width, which is with 12.5 mm the same for all experiments. The broken lines—giving the envelope—are just to guide the eyes. The figure reveals that for increasing Reynolds number the asymmetry of the flow system grows, i.e., the initially bell-shaped amplitude profile [filled (\bullet) circles] of the small-jet mode becomes more and more asymmetric and the amplitude is growing towards the cylinder ends for both branches, respectively. Increasing the Reynolds number further, the VLF mode appears on both branches at a critical Reynolds number Re_{VLF} (compare also to Fig. 6 in [15]).

Figures 7 and 8 show the amplitude A of the VLF oscillation appearing in the 10-, 12-, 14-, 16-, 18-, 20-, and 30-vortex flow, plotted versus the axial position. In each case the amplitude profile for only one branch is depicted. The measurements have been performed for Reynolds numbers slightly above the critical Reynolds numbers for the onset of the VLF oscillation. To ensure a comparison of the different flow states, all VLF amplitudes were measured in cylinders having the same aspect ratio Γ to vortex number N ratio, i.e., Γ/N was adjusted to 0.84. Thus the average wavelength of the flow is the same for all cylinders. The abscissa and ordi-

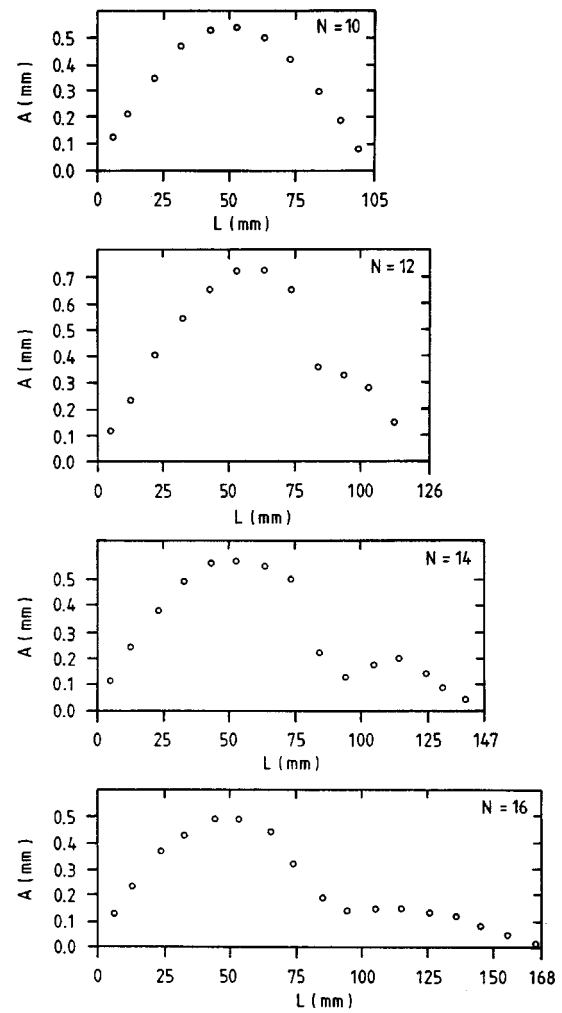


FIG. 7. Amplitude A of the VLF oscillation appearing in the 10-, 12-, 14-, and 16-vortex flow at $\Gamma/N=0.84$ plotted versus the axial position recorded just above the threshold.

nate axis of each of the seven diagrams are plotted in the same scale, respectively.

Due to the axial symmetry breaking at Re_{SJ} one expects that this symmetry breaking also appears in the symmetry of

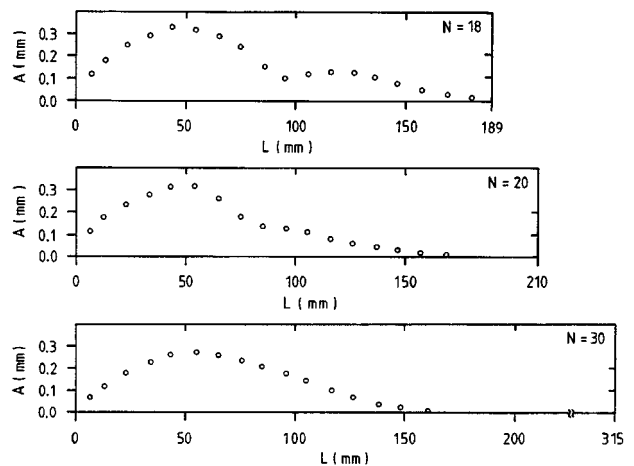


FIG. 8. The same as Fig. 7 for the 18-, 20-, and 30-vortex.

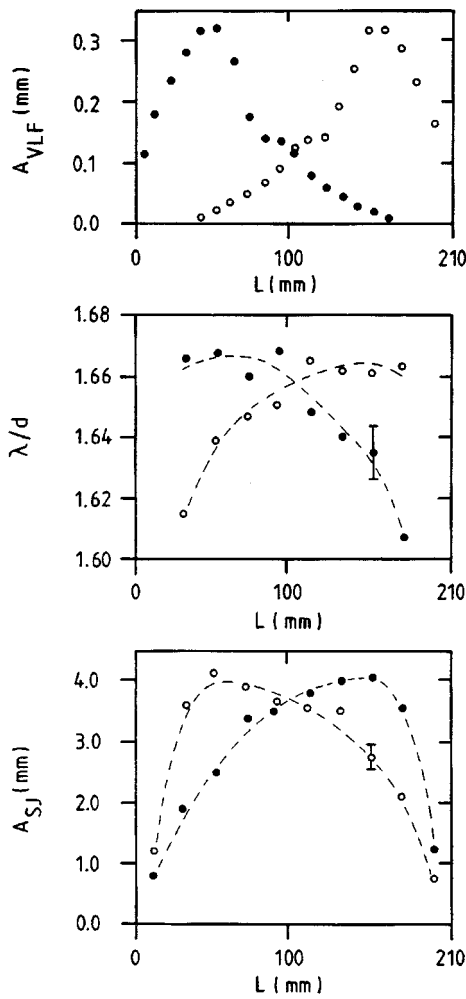


FIG. 9. Top: Profile of the VLF amplitude of both branches [one is marked with open (○), the other with filled (●) circles] for the 20-vortex flow at Reynolds number $Re=383.2$ and at $\Gamma/N=0.84$, plotted versus axial position. Middle: Corresponding distribution of the wavelengths λ/d (neglecting the wavelengths of the end-vortex pairs and recorded slightly below the onset of the VLF modes). Bottom: Corresponding profiles of the amplitude of the underlying small-jet modes (also recorded slightly below the onset of the VLF mode) plotted versus axial position.

the VLF oscillations. This is in fact the case. While the VLF-amplitude profile in the 10-vortex flow breaks the Z_2 symmetry only very weakly, the amplitude profiles depicted in Figs. 7 and 8 reveal a much stronger symmetry breaking for longer cylinders beginning with the 12-vortex flow. All VLF oscillations (including the 10-vortex flow) exhibit a maximum in amplitude at a cylinder length of approximately $L \approx 50$ mm. Furthermore, in the VLF-amplitude profile for the 12- to the 20-vortex flow one observes a strong decay of the amplitude at a length of approximately $L \approx 80$ mm. This decay separates the VLF-amplitude profile for the 12- to the 20-vortex flow into a part with larger amplitude which, apart from the height of the amplitude, shows always the same structure, and a “tail” towards larger cylinder lengths. For larger aspect ratios this separated structure passes into a smooth amplitude profile as shown in Fig. 8 for the 30-vortex flow. One result is very significant: The longer the cylinder, the more the VLF oscillations are localized towards

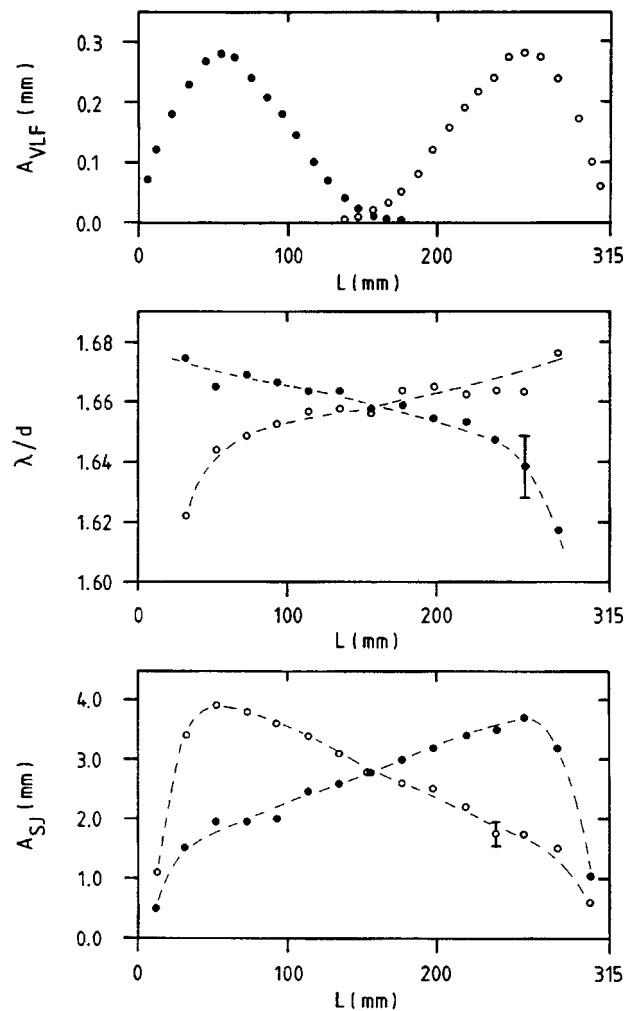


FIG. 10. The same as Fig. 9 for the 30-vortex flow.

the cylinder ends. The reason for this behavior becomes understandable by analyzing the next figures comparing the amplitude profiles of the VLF mode, the underlying small-jet mode and the corresponding distribution of axial wavelengths of the Taylor vortex structure.

In the top of Figs. 9, 10, and 11 the profiles of the VLF amplitude A_{VLF} of both branches [one is marked with open (○), the other with filled (●) circles] for the 20-, 30-, and 40-vortex flow at Reynolds number $Re=383.2$ are plotted versus axial position, respectively. In the middle, the corresponding distribution of the wavelengths λ/d (neglecting the end-vortex pairs and recorded slightly below the onset of the VLF modes), and in the bottom of Figs. 9, 10, and 11, the corresponding profiles of the amplitude of the underlying small-jet modes, which are also plotted versus axial position, are depicted. The plots of the amplitude of the VLF, the small-jet mode and the underlying wavelengths, which belong to the same branch are marked with open (○) and filled (●) circles, respectively. The broken lines are again plotted to guide the eyes. In each of Figs. 9–11 in the middle and in the bottom one error bar is depicted which indicates the maximum error of the single measurement.

These figures reveal that the VLF mode appears in those regions of the cylinder, where the amplitude of the small-jet mode is small, which is due to the shift of the wavelengths of

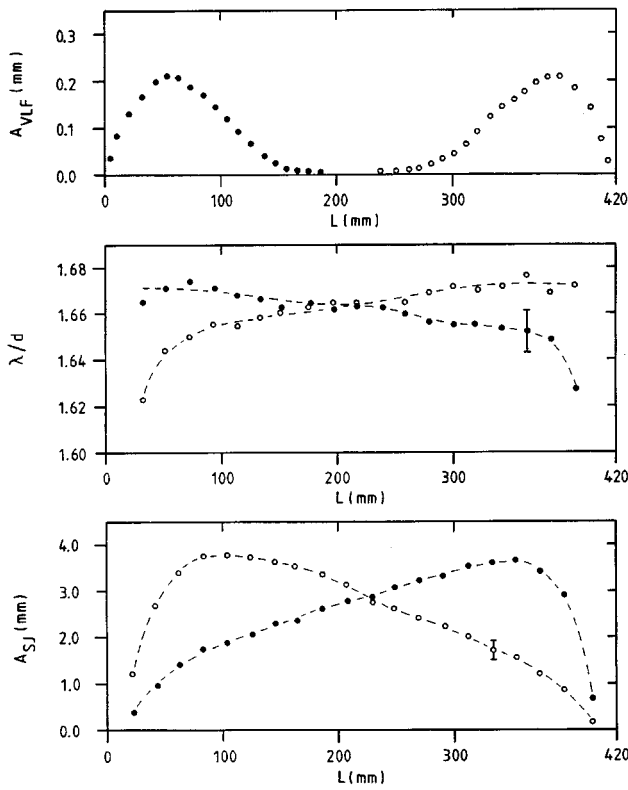


FIG. 11. The same as Fig. 9 for the 40-vortex flow.

the underlying Taylor vortices (caused by the axial symmetry breaking at onset of the small-jet mode), i.e., it appears in regions of the cylinder; where, due to the small amplitude of the small-jet mode, the coupling of neighboring small-jet oscillations is small. This is in agreement with the results we reported in a previous paper [15] for the onset of the VLF mode. After that, one observes the onset of the VLF mode if the amplitudes of neighboring oscillations in the underlying time-periodic flow modes are coupled weakly.

Figure 12 shows the evolution of the maximum height of the amplitude A_{VLF} of the VLF oscillations for successively increased cylinder lengths from the 8- to the 50-vortex flow. Again for these measurements Γ/N was adjusted to 0.84. For

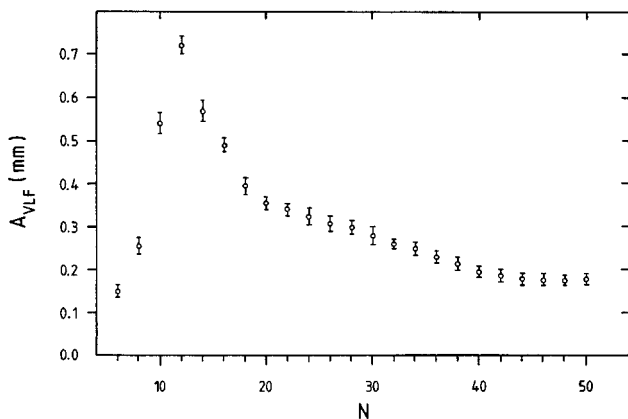


FIG. 12. Maximum height of the amplitude A_{VLF} of the VLF oscillations for successively increased cylinders from 8 to 50 vortices. For all measurements Γ/N was adjusted to an amount of 0.84.

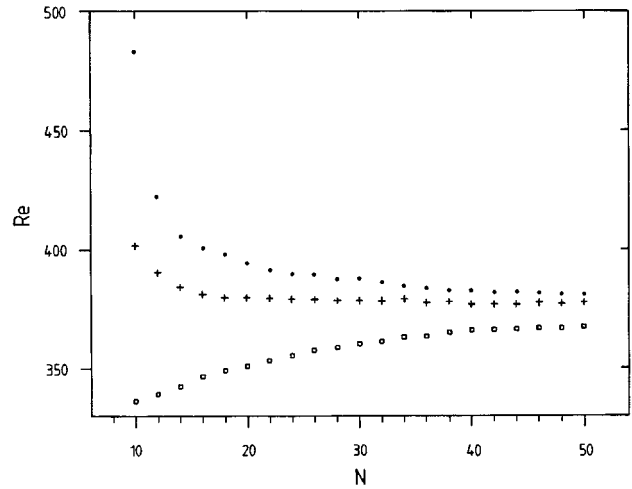


FIG. 13. Critical Reynolds numbers for the onset of the small-jet, the VLF mode and the transition to the chaotic flow, plotted for successively increased cylinders from 10 to 50 vortices at $\Gamma/N = 0.84$. For every flow with constant vortex number N three critical Reynolds numbers are depicted: The smallest, Re_{SJ} , for the onset of the small-jet mode [marked with squares (\square)], in the middle for the onset of the VLF oscillations, Re_{VLF} [marked with crosses (+)], and the largest for the transitions to chaos [marked with filled circles (\bullet)].

the 8- to the 20-vortex flow the amplitudes were measured at Reynolds numbers slightly above the onset of the VLF modes, for the larger (longer) cylinders at a Reynolds number $Re = 380.6$. The figure reveals a significant maximum at vortex number $N = 12$ and an apparently convergence for longer cylinder to a value of $A_{VLF} \approx 0.20$ mm.

Figure 13 shows the corresponding critical Reynolds numbers for the onset of these flow modes, again for successively increased cylinders from the 10- to the 50-vortex flow. For every flow with constant vortex number N three critical Reynolds numbers are depicted. The smallest, Re_{SJ} for the onset of the small-jet mode [marked with squares (\square)], in the middle the critical Reynolds number for the onset of the VLF oscillations, Re_{VLF} [marked with crosses (+)], and the largest for the transitions to chaos [marked with filled circles (\bullet)]. Obviously, the Reynolds-number ranges where the different flow states are stable, shrink for increasing cylinder lengths. Though the ranges become very narrow for large aspect ratios, they do not disappear, but showing a convergence to apparently constant Reynolds numbers.

Wave speeds in the small-jet and in the VLF flow regime

Additionally we have investigated the dependence of the azimuthal and axial wave speed of the small-jet and the VLF mode as a function of aspect ratio, respectively. Measurements of the frequency of wave speeds of traveling azimuthal waves in WVF and in MWVF in concentric cylinder systems with the inner cylinder rotating and the outer cylinder held at rest have been reported by Coles [7] and King *et al.* [38]. King and co-workers have performed measurements on the dependence of the azimuthal wave speeds s_1 of the classical Wavy mode (which they report on as WVF) and s_2 of the second traveling wave in MWVF on aspect ratio (we use the labeling for the wave speeds of the WVF and the

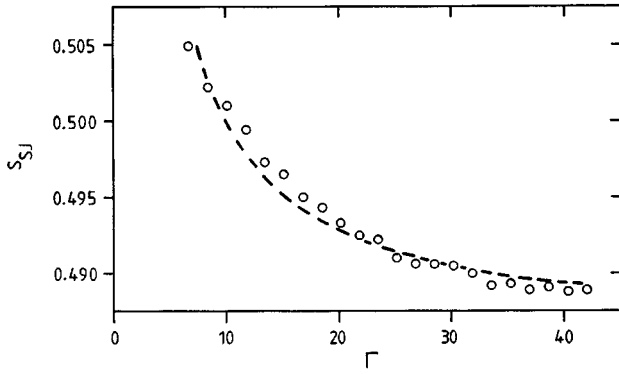


FIG. 14. Dependence of the azimuthal wave speeds s_{SJ} of the small-jet mode on aspect ratio for an average axial wavelength $\lambda/d = 1.68$ ($\Gamma/N=0.84$) recorded at Reynolds number $Re=371$ versus aspect ratio Γ . The dashed curve gives the least-squares fit to Eq. (1).

MWVF introduced by Coughlin and Marcus [21]). Their data suggested a Γ dependence of s_1 that can be described by functions that depend on $1/\Gamma$. Depicting the Figs. 14 and 15, where the dependence of the azimuthal wave speed s_{SJ} of the small-jet mode and the frequency of the VLF mode normalized to the inner cylinder rotation frequency s_{VLF} are plotted versus aspect ratio, a $1/\Gamma$ dependence of these data on aspect ratio also becomes obvious. Thus we fitted the data to the functions

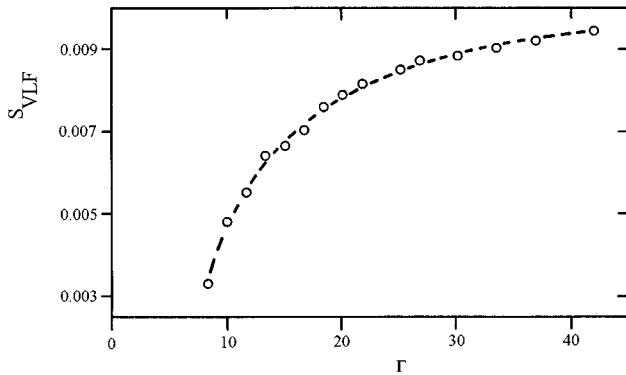


FIG. 15. Frequencies of the VLF-mode oscillations s_{VLF} normalized to the inner cylinder rotation speed versus aspect ratio for an average axial wavelength $\lambda/d=1.68$ ($\Gamma/N=0.84$), recorded at Reynolds number $Re=383$ for $N>28$ and slightly below the transition to chaos for $N<28$. The dashed curve gives the least-squares fit to Eq. (2).

$$s_{SJ}(\Gamma) = s_{SJ}(\infty) + \frac{\alpha_{SJ}}{\Gamma}, \quad (1)$$

$$s_{VLF}(\Gamma) = s_{VLF}(\infty) - \frac{\alpha_{VLF}}{\Gamma}, \quad (2)$$

which are marked with the dashed curves in the Figs. 14 and 15. The results of the least-squares fits of the data to $s_{SJ}(\Gamma)$ and $s_{VLF}(\Gamma)$ are given in Table I. The measurement errors are within the circles representing the data in the Figs. 14 and 15. A comparison of the Figs. 2 and 3 in [38] with the Figs. 14 and 15 presented here, reveals that the WVF modes, that are the Wavy mode investigated by King *et al.* and the small-jet mode investigated by us, show the same qualitative and quantitative behavior of azimuthal wave speed on aspect ratio (up to the values of the constants; see Table I), whereas it is different for the wave speed s_2 of the second traveling wave in the MWVF and the normalized frequency s_{VLF} of the VLF mode. Since the dependence of s_2 on Γ was found to be very weak (too weak to determine any functional dependence from the data) [38], the dependence of s_{VLF} yields a quite good fit to Eq. (2). This behavior also underlines the different properties of the doubly periodic axisymmetric VLF flow compared to the doubly periodic azimuthally traveling MWVF.

C. Characterization of the bifurcation towards the VLF mode

The local behavior of systems near homoclinic orbits to stationary points of saddle-focus type has been investigated numerically by Glendinning and Sparrow [39]. In their analysis they obtained explicit results how a periodic orbit approaches homoclinicity as the control parameter is varied around the value at which they had homoclinicity. Summarizing their results they found in one major case that, as the parameter μ decreases to zero, the period of the orbit through the fixed point increases to infinity [39]. They moreover deduce the equation

$$(\text{period}) \propto -(\ln \mu) \quad (3)$$

for the period of the single orbit as μ tends to zero. An experimental verification was given by Mullin and Price [40], for example.

The bifurcation diagram in Fig. 4 suggests such a behavior, since the periods of the VLF oscillations become larger and larger, reducing the Reynolds number towards the critical value for the onset of the VLF mode. This behavior was also reported in a previous paper (compare to Figs. 4 and 6 in

TABLE I. Values of the fit parameter for the aspect-ratio dependence of the wave speeds of the small-jet and the normalized frequency of the VLF mode. n is the number of data points.

Re	λ/d	n	Fit to (1)		
			$s_{SJ}(\infty)$	α_{SJ}	ξ^2
371	1.68	22	0.486	0.143	7.316×10^{-7}
Re	λ/d	n	Fit to (2)		
			$s_{VLF}(\infty)$	α_{VLF}	ξ^2
383	1.68	15	0.011	0.064	1.082×10^{-8}

^aFor flow systems having more than 28 vortices.

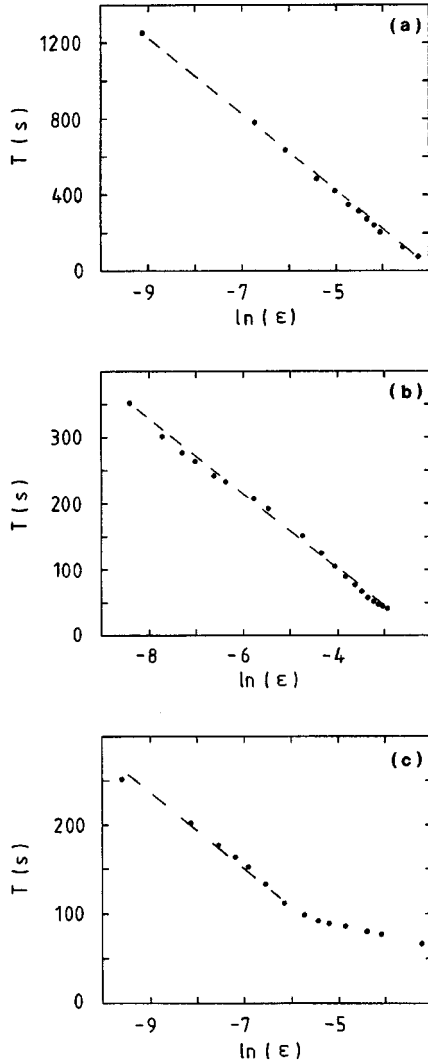


FIG. 16. Period T of different VLF-mode oscillations (a) for the 10-, (b) for the 14-, and (c) for the 20-vortex flow recorded at $\Gamma/N=0.84$, plotted versus the natural logarithm of the reduced Reynolds number ε .

[15]). Applying Glendinning's and Sparrow's model to the Taylor-Couette flow the system undergoes a homoclinic bifurcation at onset of the VLF-mode oscillations, which are homoclinic to the symmetric solution which becomes unstable at Re_{SJ} , corresponding to a solution of saddle-focus type.

Figure 16 shows the plot of the period T of different VLF modes versus the natural logarithm of the reduced Reynolds number

$$\varepsilon = \frac{\text{Re} - \text{Re}_{\text{VLF}}}{\text{Re}_{\text{VLF}}} \quad (4)$$

for the 10- [Fig. 16(a)], the 14- [Fig. 16(b)], and the 20-vortex flow [Fig. 16(c)] at $\Gamma/N=0.84$. Re_{VLF} is again the critical Reynolds number for the onset of the VLF mode. The figure reveals that the smaller the aspect ratio of the flow, the better Eq. (3) is satisfied. While the linear fit in Fig. 16(a) is quite satisfactory, the curve of the plot of the period versus reduced Reynolds number becomes slightly nonlinear in the

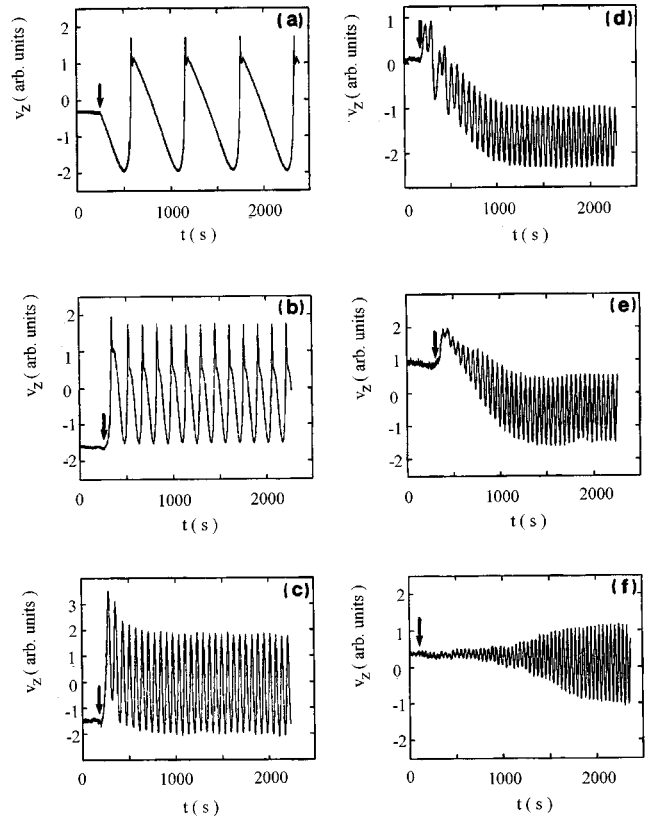


FIG. 17. Buildup of the VLF-mode oscillations (a) in 12-, (b) in 14-, (c) in 16-, (d) in 20-, (e) in 24-, and (e) in 42-vortex flow after a small jump in Reynolds number from $\varepsilon=-0.006$ to $\varepsilon=+0.006$ over the critical value for the onset ($\Gamma/N=0.84$). The scaling in the axial velocity v_z is different, thus one cannot compare the amplitude heights of the different flow states due to these measurements.

logarithmic plot in Fig. 16(b) and in Fig. 16(c) a linear fit only very close to the critical Reynolds number makes sense. This behavior continues with increasing cylinder length until the homoclinic behavior disappears.

From the measurements it is not possible to state whether the homoclinic bifurcation at onset of the VLF mode disappears in 20-, 22-, etc., or at 30-vortex flow, because the change to a different behavior is not sharp. The analysis of the experimental results only reveals that from the plots in Fig. 16 it becomes convincing that the transition is homoclinic up to 20-vortex flow.

To analyze the bifurcation to the VLF mode additionally, we compare the buildup of this time-dependent mode after a small sudden jump above the critical Reynolds number in small and large aspect-ratio systems. Hence Fig. 17 shows this buildup of the VLF oscillations in 12- [Fig. 17(a)] up to the 42-vortex flow [Fig. 17(f)], all recorded for a flow with $\Gamma/N=0.84$. The small jump in Reynolds number above the critical value is marked with an arrow in the figures. They reveal the quite different behavior of the small and large aspect ratio systems.

Though we find a continuous increase in frequency with increasing values of Γ , indicating that we deal with the same flow mode, Fig. 15, the behavior at onset changes qualitatively: The transition to VLF mode at small Γ as a sudden onset to full amplitude—identified as homoclinic behavior—while for large Γ the buildup of the amplitude displays a

dynamic behavior one would expect for a Hopf-type bifurcation [11].

Furthermore, the VLF oscillations in 12-, 14-, and 16-vortex flow have a zigzag structure whereas it is apparently sinusoidal in the larger flow systems. This behavior has another consequence, which we focus on in Sec. VII.

VI. PERIOD DOUBLING ON A TORUS

Until now we have presented an experimental study of an additional “main sequence” to chaos in Taylor-Couette flow, which is valid for wide wave-number and aspect-ratio ranges in Taylor-Couette flow (with radius ratio $\eta=0.5$) and we thus stated that it may display a “general” behavior in this flow system. After analyzing the onset of time dependence and the transition to the VLF regime in 10- to 50-vortex flow, we now concentrate on the transition to chaos. It is amazing that, again, the flow exhibits the same scenario as a transition to chaos in a wide parameter range, i.e., from 10- to 50-vortex flow (and for $\lambda < 1.78d$) the flow shows a period-doubling-on-a-Torus route to chaos. Such scenarios have been measured in 8-, 10-, 14-, 18-, 20-, 24-, 30-, and 34-vortex flow. Detailed measurements in 40- or even in 50-vortex flow are hard to perform, because transients become very long; in fact the relaxation time of the system grows with L^2 [41], i.e., in our system for the onset of the first period doubling up to approximately 70 h in 50-vortex flow. In these systems (40–50 vortices) only the first period doubling of the VLF oscillation was measured to confirm that the transition to chaos is the same in all considered flow systems, so we conject that the transition to chaos are also determined by period-doubling-on-a-Torus routes as measured in the smaller aspect-ratio systems.

Experimental evidence for period-doubling-on-a-Torus has been reported, for example, in the following systems: In an electrochemical reaction [42], convecting molten gallium bounded by a rectangular box [43], a double pendulum [44], and in an annular array of Raleigh-Bénard convection pattern [45]. Another experiment [46] was reported in [45]. The entire scenario had only been observed by Skeldon and Mullin [44] and by Flesselles *et al.* [45]. Theoretical investigations have been made by Skeldon and Mullin [44], Franceschini [47], Kaneko [48], and Arnéodo *et al.* [49]. Skeldon and Mullin, in addition to their experimental investigations, studied numerically the equations of motion of a parametrically excited double pendulum which they derived from the Lagrangian, Franceschini found Torus-doubling bifurcations in a truncated mode expansion of the Navier-Stokes equation, Kaneko has published a numerical study of Torus-doubling cascades in coupled maps, and Arnéodo *et al.* studied numerically a periodically forced normal form known to exhibit a period-doubling cascade.

The onset of the Torus doubling occurs with the appearance of the subharmonic $\omega_{\text{VLF}}/2$ of the lowest frequency ω_{VLF} in the velocity power spectrum. This is shown in Figs. 18–21, where eight different axial velocity power spectra at the transition to chaos of a doubly periodic flow consisting of small-jet and VLF mode at aspect ratio $\Gamma=16.8$ ($\Gamma/N=0.84$) are depicted, for example. Only the doublings of the VLF mode in the spectrum are shown, because the peak of the

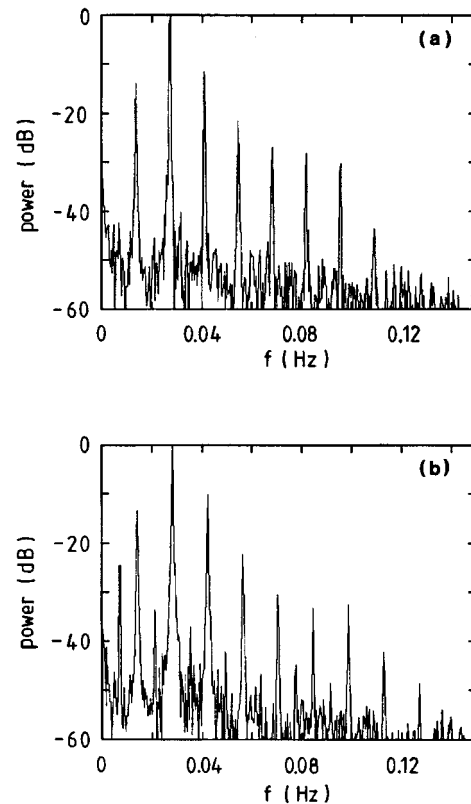


FIG. 18. Axial velocity power spectra of a period-doubling-on-a-Torus scenario in 20-vortex flow slightly below the transition to chaos of a doubly periodic flow consisting of small-jet and VLF mode at aspect ratio $\Gamma=16.8$ ($\Gamma/N=0.84$). Only the doublings of the VLF mode in the spectrum are depicted; (a) The velocity power spectrum of a period-2 torus at Reynolds number $\text{Re}=389.3$; (b) a period-4 torus at $\text{Re}=392.7$.

much faster small-jet mode appears at approximately $\omega_{\text{SJ}} \approx 2.2$ Hz in the power spectra and thus, depicting the whole spectra, the period-doubling peaks of the VLF mode would lie too close to be observable. The power spectra were calculated from time series having 1 048 576 data points (apart from the time series recorded for Fig. 19, which has only 262 144 data points, reflected in the worse resolution of the power-spectrum plot). Figure 18 shows the velocity

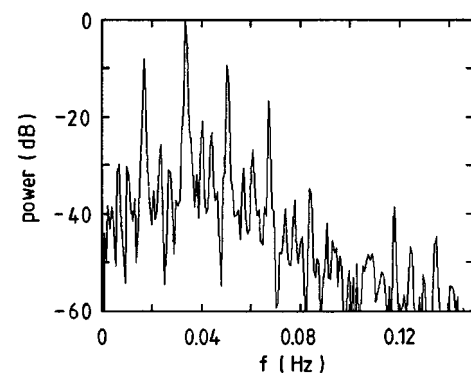


FIG. 19. The same as Fig. 18 for a flow at the transition point to chaos at $\text{Re}=393.1$. Here the period-4 and the period-8 peaks are disturbed.

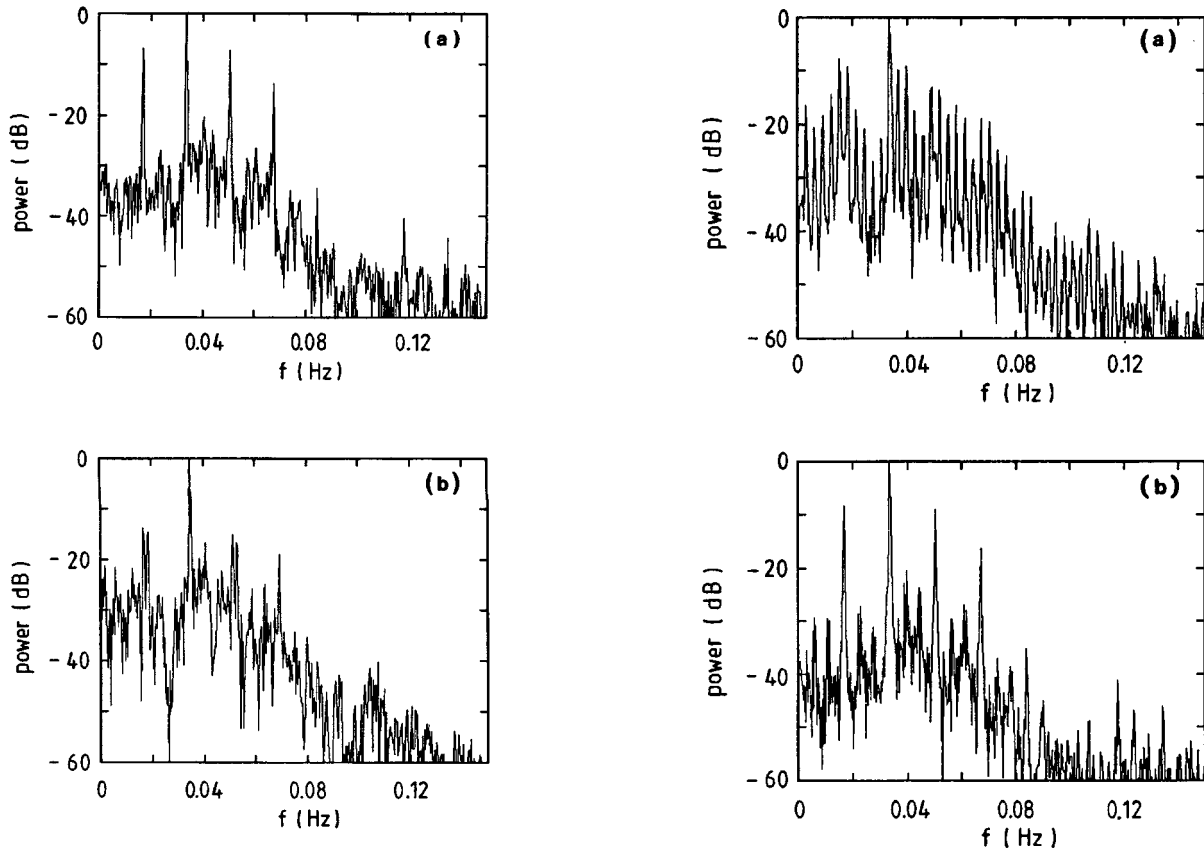


FIG. 20. The same as Fig. 18 for (a) a chaotic flow at $Re=394.9$ where the period-4 peaks are disappeared and (b) a chaotic at $Re=395.1$ where the period-2 peaks are split.

power spectra of a period-2 torus at Reynolds number $Re=389.3$ [Fig. 18(a)] and a period-4 torus at $Re=392.7$ (b).

In Fig. 19 at $Re=393.1$ the appearance of additional period-4 and period-8 peaks in the power spectrum can be seen. The period-4 and period-8 peaks are split. Such splittings of the subharmonics has been found experimentally by Pfister [50], who explained this feature by a coupling of different time-periodic flow modes present in a very small 2-vortex Taylor-Couette system corresponding to theoretical investigations by Horner [51] who studied the effect of a periodic perturbation on a nonlinear dynamic system undergoing a sequence of period doublings, numerically. Horner assumed that the degrees of freedom responsible for the period doubling are coupled to a weak external periodic perturbation of unknown origin or to other oscillating internal degrees of freedom which are observed otherwise in the system. Applying this model to the doubly periodic flow consisting of small-jet and VLF mode, the VLF mode is responsible for the period doublings and is coupled weakly to the underlying small-jet mode, which corresponds to the weak external periodic perturbation. To demonstrate such a dynamical behavior Horner has studied a one-dimensional map exhibiting a period-doubling sequence which he coupled to a periodic function and found splittings of the subharmonics in the corresponding power spectra. Additionally he found that the periodic perturbation destroys higher bifurcations. This is in accordance with our experimental observations where we never found higher subharmonics than those corresponding to a period-8 in the doubling cascade

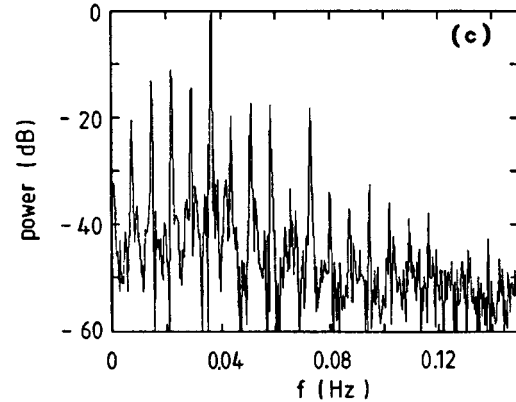


FIG. 21. The same as Fig. 18 for (a) a period-11 window at $Re=394.4$, (b) a period-6 window at $Re=395.0$, and (c) a period-5 window at $Re=395.3$.

prior to the first onset of chaos. After passing the critical Reynolds number the flow undergoes an inverse cascade, whereby the subharmonics disappear after splitting. This is shown in Figs. 20(a) and 20(b) where first [Fig. 20(a)] the period-4 and period-8 peaks disappeared and then the period-2 peaks are split [Fig. 20(b)]. Figures 21(a)–(c) shows three examples of periodic windows, (a) a ‘‘period-11 window’’ at $Re=394.4$, (b) a ‘‘period-6 window’’ at $Re=395.0$, and (c) a ‘‘period-5 window’’ at $Re=395.3$. Due to the intensities of the subharmonic peaks we identify the state in Fig. 21(b) as a period-6 window and not as a doubled period-3 window. According to the simple model of the one-dimensional logistic equation the period-11 window should appear for higher Reynolds numbers than the period-6 and

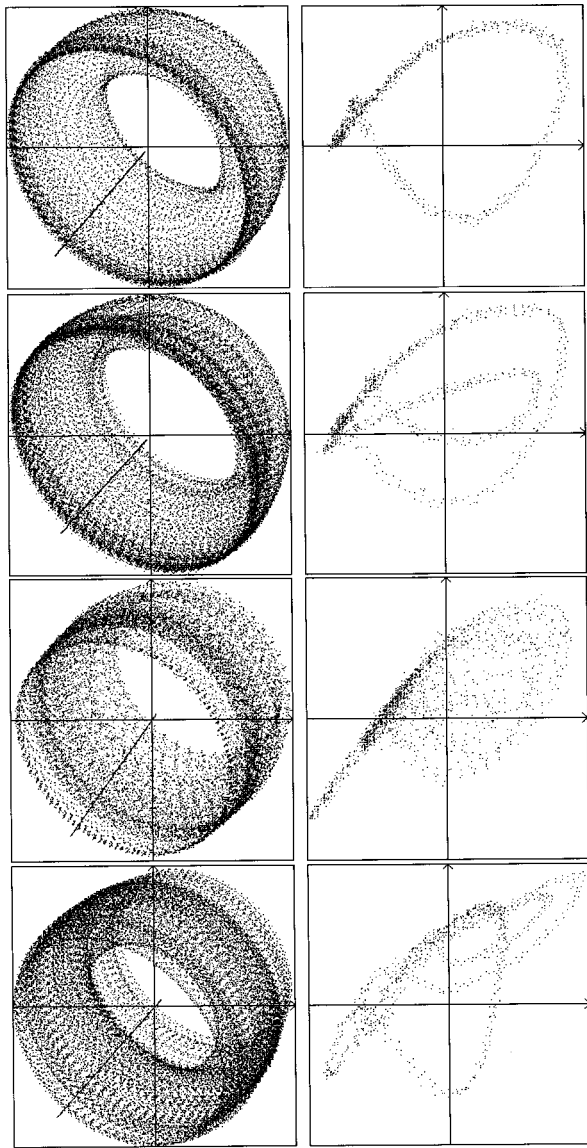


FIG. 22. A period-doubling-on-a-torus scenario in 14-vortex flow at aspect ratio $\Gamma=11.76$ ($\Gamma/N=0.84$). Left column: Projections of three-dimensional reconstructions of the attractors in phase space. Right column: The corresponding Poincaré sections as indicated by the line in the third quadrant in the left figures. From the top to the bottom the simple torus, consisting of small-jet and VLF mode, at $Re=410$, the doubled torus at $Re=418$, a chaotic attractor at $Re=422$, and an attractor recorded in a period-3 window at $Re=423$.

period-5 windows, but one should not overestimate this model. Further analysis of period doubling routes to chaos in a very small annulus having two vortices have shown that this simple model is not suitable to describe the dynamics of the period doublings to chaos even in such a small system where the dynamics is expected to be simpler than in larger aspect ratios [52,53].

Another example is given in Fig. 22 where a period-doubling-on-a-torus scenario in 14-vortex flow at aspect ratio $\Gamma=11.76$ ($\Gamma/N=0.84$) is shown by exhibiting the two-dimensional projections of the reconstructions of the attractors in phase space in the left column and the corresponding Poincaré-sections of these attractors in the right column.

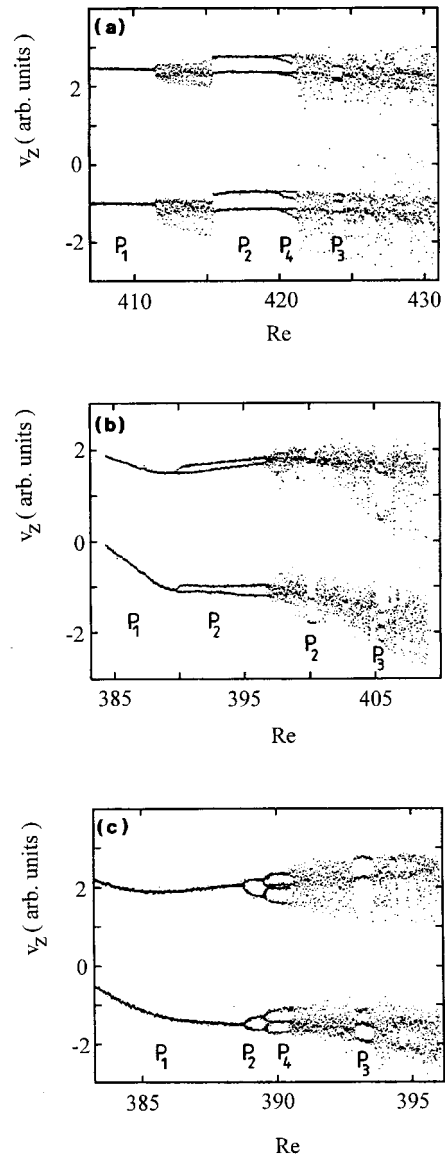


FIG. 23. Bifurcation cascades of period-doubling-on-a-torus scenarios to the chaotic regime for three different flow systems. The underlying small-jet mode was filtered and only the successive extrema of the axial velocity component v_z are plotted while the Reynolds number is ramped quasistatically (a) A bifurcation diagram of the 14-vortex flow for $\Gamma=11.76$ ($\Gamma/N=0.84$), where the Reynolds number was increased quasistatically within $\Delta Re/\Delta t=1.63 \times 10^{-4} \text{ s}^{-1}$, (b) the bifurcation diagram of the 20-vortex flow for $\Gamma=16.8$ ($\Gamma/N=0.84$), the Reynolds number was increased quasistatically within $\Delta Re/\Delta t=3.26 \times 10^{-4} \text{ s}^{-1}$, and (c) shows a bifurcation diagram of the 24-vortex flow for $\Gamma=20.16$ ($\Gamma/N=0.84$). The Reynolds number was increased quasistatically within $\Delta Re/\Delta t=1.63 \times 10^{-4} \text{ s}^{-1}$.

From the top to the bottom the torus, consisting of small-jet and VLF mode, at $Re=410$, the doubled torus at $Re=418$, a chaotic attractor at $Re=422$, and an attractor recorded from a time series recorded in a period-3 window at $Re=423$.

In Fig. 23(a)–23(c) bifurcation cascades to the chaotic regime are shown for three different flow systems. Here the underlying small-jet mode was filtered and only the successive extrema of the axial velocity component v_z were plotted

while the Reynolds number was ramped quasistatically within $\Delta Re/\Delta t \approx 3 \times 10^{-4} \text{ s}^{-1}$. Figure 23(a) shows a bifurcation diagram of a period-doubling-on-a-torus scenario in the 14-vortex flow for $\Gamma=11.76$ ($\Gamma/N=0.84$). The figure reveals period doublings up to period-4 and a periodic period-3 window in the chaotic regime. Obviously the bifurcation from period-1 to period-2 is chaotic, which is a characteristic for the smaller flow systems from 10 up to 16 vortices. In Fig. 23(b) the bifurcation diagram of a period-doubling-on-a-torus scenario in the 20-vortex flow for $\Gamma=16.8$ ($\Gamma/N=0.84$) is depicted. Prior to the onset of chaos at $Re=396.8$ the flow exhibits a doubling cascade up to period-2. Two periodic windows with period-2 at $Re=400$ and with period-3 at $Re=405$ are visible. Figure 23(c) finally shows a bifurcation diagram of a period-doubling-on-a-torus scenario in the 24-vortex flow for $\Gamma=20.16$ ($\Gamma/N=0.84$). This flow shows a doubling cascade up to period-4 before it becomes chaotic and a wide period-3 window in the chaotic regime at $Re \approx 393$. The figures reveal that, first, the Reynolds-number ranges of the doubling sequences become more and more narrow for increasing cylinder length, which was expected from Fig. 13 where one observes that the Reynolds-number ranges of occurrence of the different flow states shrink for increasing cylinder lengths, and secondly, the doublings become more and more “perfect” though they are more and more difficult to record, because the length of the transients grows quadratically with cylinder length. Due to this fact it becomes nearly impossible to record such doubling sequences for even longer cylinders.

Figure 24(a) and 24(b) shows two bifurcation diagrams of the period-doubling-on-a-torus scenario in a flow with the same vortex number N , here $N=14$, but for slightly different aspect ratios to demonstrate the strong dependence of the bifurcation sequences on the geometrical boundary conditions. For these recordings the Reynolds number was increased quasistatically within $\Delta Re/\Delta t \approx 3 \times 10^{-4} \text{ s}^{-1}$. From Fig. 24(a) to Fig. 24(b) the cylinder length was increased from $L=146.9 \text{ mm}$ to $L=147.2 \text{ mm}$, respectively. This yields aspect ratios $\Gamma=11.752$ ($\Gamma/N=0.8394$) for the flow shown in Fig. 24(a) and $\Gamma=11.776$ ($\Gamma/N=0.8411$) for the flow shown in Fig. 24(b). While the period-2 range is relative robust against this small changes in cylinder length, the period-4 sequences and the periodic windows in the chaotic regime are very sensitive to the change of the boundary conditions, which is expected for chaotic flows.

To demonstrate the measured structure of the periodic windows, in Fig. 25(a) the doubling sequence which was formerly depicted in Fig. 23(b) is shown with extensions of the regime around the two visible periodic windows. Figure 25(b) reveals a doubling from period 2 to period 4 and in the second periodic window a doubling from period 3 to period 6 becomes visible. These doublings are not observable in Fig. 25(a), which is due to the velocity $\Delta Re/\Delta t$ with which the time series are recorded. While the extended plots are recorded within $\Delta Re/\Delta t = 3.12 \times 10^{-5} \text{ s}^{-1}$ the bifurcation diagram in Fig. 25(a) was recorded within $\Delta Re/\Delta t = 3.26 \times 10^{-4} \text{ s}^{-1}$, i.e., approximately ten times faster than for the extensions of the periodic windows. This demonstrates the sensitivity of the recordings on the ramping rate and on the transients which increase strongly with increasing cylinder length. This also explains why the period doubling in the

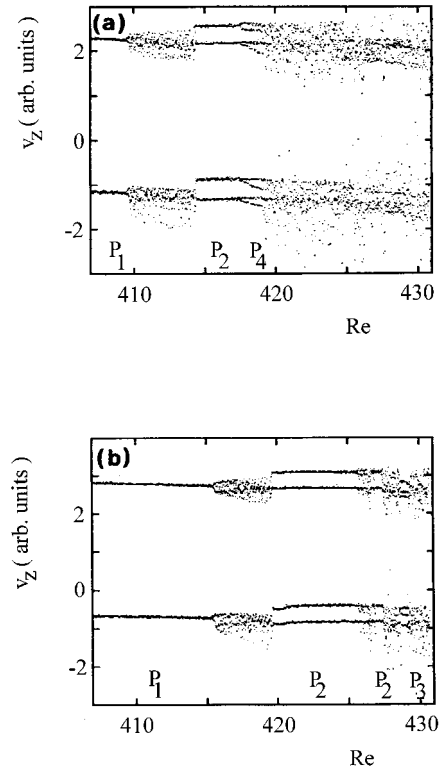


FIG. 24. Two bifurcation diagrams of period-doubling-on-a-torus scenarios in the 14-vortex flow recorded for slightly different aspect ratios. Only successive extrema of the axial velocity component v_z are plotted while the Reynolds number is ramped quasistatically. For these recordings the Reynolds number was increased quasistatically within $\Delta Re/\Delta t = 1.63 \times 10^{-4} \text{ s}^{-1}$. The diagram shown in (a) was recorded at $L=146.9 \text{ mm}$ ($\Gamma/N=0.8394$), in (b) at $L=147.2 \text{ mm}$ ($\Gamma/N=0.8411$).

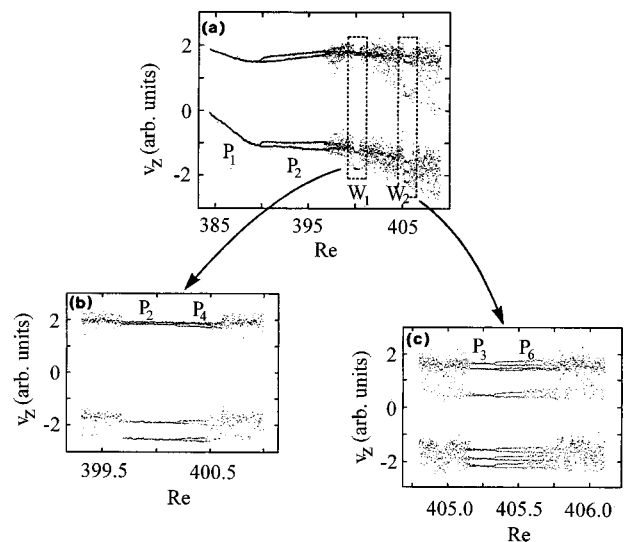


FIG. 25. The doubling sequence which was formerly depicted in Fig. 23(b) is shown with extensions of the regime around the two visible periodic windows. (b) reveals a doubling from period-2 to period-4 and in (c) a doubling from period-3 to period-6 becomes visible. The extended plots are recorded within $\Delta Re/\Delta t = 3.12 \times 10^{-5} \text{ s}^{-1}$.

structure of the VLF-mode oscillations cannot be observed in the bifurcation diagram in Fig. 4.

VII. QUANTITATIVE CHARACTERIZATION OF THE TRANSITION TO CHAOS

Many methods are available to characterize time series measured on nonlinear dynamical systems. So one can calculate power spectra using methods like fast-Fourier-transform (FFT) algorithms as shown in the last section (Figs. 18–21). But these methods based on linear system theory are limited giving a quantitative characterization of the transition to chaos, estimating the critical Reynolds number for such a transition or comparing different chaotic time series.

More detailed results to characterize the transition to chaos can be obtained with powerful methods developed within the theory of nonlinear systems. These mathematical methods, which are state of art, cannot be described in detail here. So we restrict the mathematical review to a brief summary of the methods we actually applied here. To classify the time series

$$\{\nu_z(t_s)\}, \quad s \in \{1, \dots, N_{\text{dat}} - (d_E - 1)\tau/T_a\}, \quad (5)$$

where d_E is the embedding dimension, N_{dat} the number of sampled data points, τ the delay time, and T_a the sampling time, one first reconstructs the phase space (or rather embedding space) of the nonlinear dynamical system. We used Takens' delay time coordinates [54], where a vector in the embedding space is given by

$$\vec{x}(t_s) = (\nu_z(t_s), \nu_z(t_s + \tau), \dots, \nu_z(t_s + \tau(d_E - 1))). \quad (6)$$

For convenience we shall write \mathbf{x}_s instead of $\mathbf{x}(t_s)$.

To find optimal embedding parameters, i.e., the proper delay time τ and a sufficiently large embedding dimension d_E , one has to calculate the fill factor $f_{d_E}(\tau)$ (a measure of the utilization of the embedding space in any embedding dimension) or the integral local deformation $\Delta_{d_E}(\tau)$ (a measure of the homogeneity of the local flow).

The fill factor is defined by

$$f_{d_E}(\tau) := \log_{10} \left(\frac{1}{N_{\text{ref}}} \frac{\sum_{k=1}^{N_{\text{ref}}} V_{d_E k}(\tau)}{\langle V_{d_E} \rangle} \right), \quad (7)$$

where $V_{d_E k}(\tau)$ is the volume of the k th parallelepiped defined by $(d_E + 1)$ corner points which are arbitrarily distributed on the attractor, $\langle V_{d_E} \rangle$ is a normalization by the minimum enclosing box of the attractor in each embedding dimension d_E and N_{ref} is the number of reference points. The first maxima of the fill factor, corresponding to maximum spanned attractors in the embedding space, provide proper delay times. A sufficiently large embedding dimension can be obtained by the convergency of the qualitative structure of the fill factor for successively increasing embedding dimension. A detailed description of this method can be found in [55–57].

To define the integral local deformation $\Delta_{d_E}(\tau)$ one calculates the evolution of successive distances between a reference point and the center of mass of neighboring points

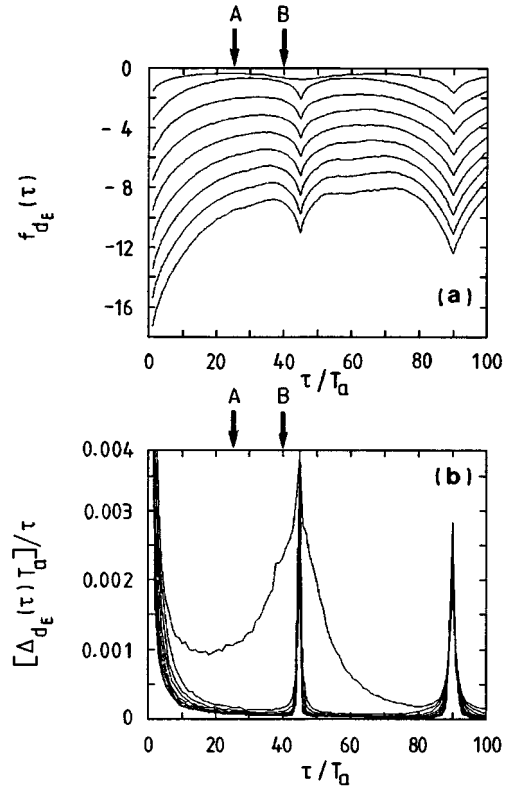


FIG. 26. Fill factor (a) and averaged integral local deformation (b) versus delay time τ normalized to the sampling rate T_a for embedding dimensions $d_E=2-12$ for a time series recorded at $\text{Re}=384$ taken from the scenario shown in Fig. 25(a).

when time proceeds. In an optimal reconstruction, for which we require homogeneity of the local flow, points on neighboring trajectories remain neighboring for small evolution times. The first minima of $\Delta_{d_E}(\tau)$, corresponding to a maximum homogeneity of the local flow, provide proper delay times; the embedding dimension can be obtained from the convergency at these minima. For details see [56].

Figure 26(a) illustrates the fill factor for a state recorded at $\text{Re}=384$ in 20-vortex flow for $\Gamma/N=0.84$. The time series is taken from the scenario shown in the bifurcation diagram in Fig. 25(a). $f_{d_E}(\tau)$ was calculated for embedding dimensions $d_E=2-10$ and delay times $\tau/T_a=0-100$ (T_a is the sampling rate of the digitally recorded time series). The intervals between the arrows A and B indicate proper delay times. Figure 26(b) shows the calculation of the corresponding integral local deformation (ILD). The figure showing the ILD is plotted in the same interval as the fill factor. $\Delta_{d_E}(\tau)$ is normalized by τ/T_a , which is often convenient for chaotic time series [56,58]. The result of this calculation agrees with the result obtained from the fill factor, i.e., the local flow is homogeneous when the attractor is maximum spanned. The figure reveals that there is a wide τ range for each state which yields sufficient delay times for the calculation of the corresponding attractor invariants, again indicated by the interval made by the arrows A and B. The time series is recorded in the beginning of the scenario depicted in Fig. 25(a). Evaluations of the fill factor and ILD for higher Reynolds numbers are quite similar, so that one can choose the same optimal embedding parameter for all data sets for the

reconstructions used to characterize the scenario.

To estimate the fractal dimension of the reconstructed strange attractors in phase space we calculate the correlation dimension D_2 [59]

$$C(R) \propto R^{D_2} \rightarrow D_2 = \lim_{R \rightarrow 0} \frac{\log_{10}[C(R)]}{\log_{10}(R)}. \quad (8)$$

R is the scaling radius and $C(R)$ is the correlation integral,

$$C(R) \approx \frac{1}{N_{\text{ref}}} \sum_{j=1}^{N_{\text{ref}}} \frac{1}{N_{\text{dat}}} \sum_{i=1}^{N_{\text{dat}}} \sigma(R - \|x_i - x_j\|), \quad (9)$$

where σ is the Heaviside function, N_{dat} is the number of points in phase space, and $N_{\text{ref}}=3000$ is a sufficiently large number of reference points.

Even in the laminar flow regime the phase dynamics of the VLF mode leads to a very disproportionate density of the flow in phase space on the torus surface. Considering the reconstructed attractor in phase space and the corresponding Poincaré section of the state depicted in the top of Fig. 22, one sees that the density of points is much higher in the upper-left quadrant than in the other three quadrants of the graph showing the Poincaré section. This is due to the fact that the VLF oscillation, especially in the smaller cylinders, is not sinusoidal but shows a ‘‘zigzag’’ structure as depicted in Figs. 3(a) and 3(b), for example. While the oscillation only needs approximately 15 sec to go through the steep slope of the periodic curve it needs about 9200 sec to go through the flat slope in Fig. 3(a), whereas in Fig. 3(b) the rising lasts about 120 secs. This dynamical behavior, of course, is reflected in the dynamics in phase space, leading to an underestimation of the fractal dimension by calculating the correlation dimension D_2 , because during the slow rising the dynamics in phase space is similar to a limit cycle moving very slowly. An estimation of the correlation dimension after Grassberger and Procaccia yields a value of $D_2=1.85 \pm 0.08$ for the state in 14-vortex flow depicted in the top of Fig. 22, and the calculation of the local slope of the correlation integral for the chaotic state depicted in the third row of Fig. 22 shows no convergence, for example.

From this point of view fortunately the structure of the VLF oscillations changes for increasing cylinder length to a more sinusoidal oscillation, as shown in the comparison in Fig. 17 between the 12-, 14-, 16-, 20-, 24-, and 40-vortex flow. Therefore for vortex numbers larger or equal than 20 it becomes possible to perform such calculations.

Figure 27 illustrates the results obtained from two experimental attractors. The first time series is recorded below ($\text{Re}=395.7$), and the second above ($\text{Re}=397.4$) onset of chaos. In Fig. 27(a) the double logarithmic plot of the correlation integral versus radius is shown for $\text{Re}=395.7$, in Fig. 27(c) for $\text{Re}=397.4$. The radius is given in per cent of the global attractor extension. Both attractors contain $N_{\text{dat}}=262\,144$ data points in the resolution of a 14-bit ADC. We chose $N_{\text{ref}}=3000$ reference points for an estimate of the correlation integral. In the plots $C(R)$ is drawn for embedding dimensions $d_E=1-12$. The dashed lines illustrate the fit of the slopes yielding the correlation dimension D_2 . For $\text{Re}=395.7$ one obtains $D_2 \approx 2.21 \pm 0.09$; for $\text{Re}=397.4$: $D_2 \approx 2.46 \pm 0.11$. Obviously one cannot perform the required limit $R \rightarrow 0$ for

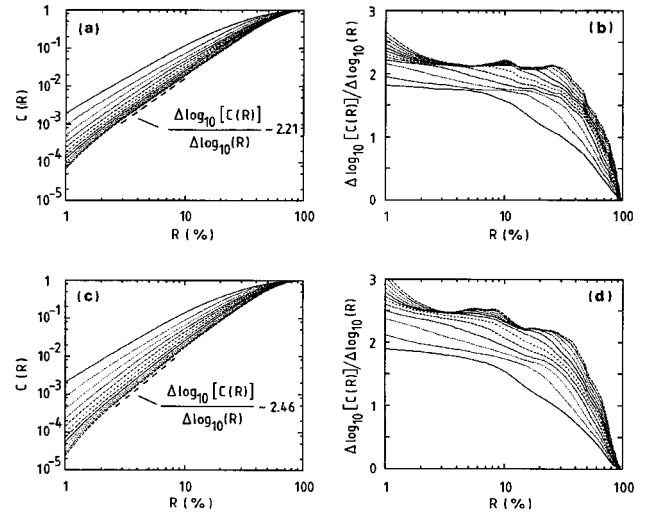


FIG. 27. Double-logarithmic plotted correlation integrals $C(R)$ (left column) and the corresponding local slopes (right column) versus scaling radius R from $d_E=2-12$ for $\text{Re}=395.7$ [(a) and (b)] and $\text{Re}=397.4$ [(c) and (d)] for two different time series taken from the scenario shown in Fig. 25(a).

the dimension calculation, because due to noise one finds a ‘‘knee’’ in the double logarithmic $C(R)$ plots at approximately $R=3\%$. Below that value the trajectories tend to fill the embedding space in any dimension, leading to a correlation dimension $D_2=d_E$. Above this ‘‘knee’’ the fractal geometry of the strange attractor can be detected. In Figs. 27(b) and 27(d) the local slopes (i.e., D_2) of the correlation integral, plotted as a function of the scaling radius R , are depicted. Both plots show an interval corresponding to the linear fit of the slopes in the $C(R)$ plots. For $\text{Re}=395.7$ in an interval between $R=3$ and 7% and for $\text{Re}=397.4$ in an interval between $R=3$ and 4% D_2 shows sufficient convergence, yielding the correlation dimension D_2 .

The calculated results for the fractal dimension are of small significance when they are not discussed as a function of Reynolds number and boundary conditions of the system. Figure 28 shows that the evolution of the correlation dimension D_2 yields a useful quantitative characterization of the period-doubling-on-a-torus route recorded in 20-vortex flow for $\Gamma=16.8$ ($\Gamma/N=0.84$). Figure 28(a) shows this period-doubling-on-a-torus scenario [also depicted in Fig. 25(a)] and Fig. 28(b) the corresponding evolution of the correlation dimension as a function of Reynolds number. From $\text{Re} \approx 384$ to $\text{Re} \approx 390$ one finds a period-1 torus. At $\text{Re} \approx 390$ a period-doubling bifurcation appears, leading to a period-2 torus, and at $\text{Re} \approx 396.8$ the transition to chaos occurs. From $\text{Re} \approx 384$ to $\text{Re} \approx 390$ the estimated correlation dimension is $D_2 \approx 2$, as expected, whereas between $\text{Re} \approx 390$ and $\text{Re} \approx 396$, where the doubled torus appears, the estimated correlation dimension takes values between $D_2 \approx 2.15$ and $D_2 \approx 2.2$. For this state one also would expect an estimated value of $D_2 \approx 2$, but this increase of the calculated value is obviously due to the fact that the trajectories of both tubes of the doubled torus come very close to each other in some regions in phase space, following that the value of the correlation integral $C(R)$ is locally increased in these regions, because the Grassberger-Procaccia algorithm counts more neighboring points of a

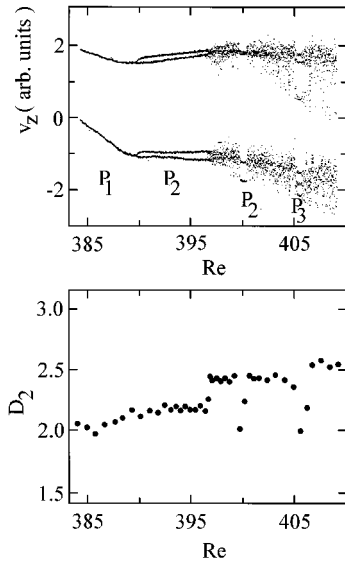


FIG. 28. (a) Period-doubling-on-a-torus scenario depicted in Fig. 25(a). (b) corresponding evolution of the correlation dimension as a function of Reynolds number.

given reference point N_{ref} and scaling radius R compared to regions in phase space where both tubes of the doubled torus are sufficiently separated. At $Re_{\text{VLF}}=396.8$ the transition to chaos occurs going along with a sudden jump in the correlation dimension to $D_2 \approx 2.45$. Up to the two periodic windows at $Re \approx 400$ and $Re \approx 405$, where the estimated correlation dimension is in agreement with the expected values, this value of D_2 keeps nearly unchanged. After the second periodic window at $Re \approx 405$ there is a second (sudden) increase of the correlation dimension to $D_2 \approx 2.55$.

VIII. DISCUSSION AND CONCLUSION

We have presented an experimental study of the very-low-frequency VLF mode, a very slow time-periodic oscillation with azimuthal wave number $m=0$ in axisymmetric Taylor-Couette flow. First results of the interaction of VLF-mode oscillations with different underlying time-periodic Taylor vortex flow (WVF) modes concentrating on smaller aspect ratios—especially the 10-vortex flow—covering the entire wavelength range of the underlying Taylor vortex flow had been previously reported in [15,34].

The measurements presented here cover a parameter range that reaches from the onset of time-dependence via the onset of the VLF mode to the transition to chaos in the wavelength range $\lambda < 1.78d$ (d is the gap width of the cylinder) appearing in flow systems having 10–50 vortices.

The VLF mode qualitatively and quantitatively differs from all other known time-periodic flows in the Taylor-Couette system. It always occurs as a secondary or higher time-dependent instability. It was shown that its occurrence depends on the strength of the spatial coupling of the oscillations in neighboring vortex pairs of the underlying WVF modes.

All experimental observations support the conjecture that there is a *causal connection between the appearance of the VLF mode* and the presence of the underlying time-periodic flow modes. At onset of the VLF mode one observes a

“breakdown” of the azimuthal wave coherence of the underlying time-periodic Taylor vortex flow, and we argue that this shift of the phases of oscillations in neighboring vortices causes the occurrence of the VLF mode: The interaction of the VLF mode with the underlying time-periodic flow modes reveals that the VLF mode is *caused by the strength of coupling of the phases of the underlying time-periodic flow modes*. These modes cause a variation of the wavelength of the vortices in the flow. But there is still a coupling between these modes and an axial phase diffusion. Furthermore the wave speeds of the time-periodic flow modes depend on the wavelength of the vortices. Due to this a local disturbance of the wavelength leads to a change in the wave speed. A shift of the phases between the oscillations of neighbouring vortices occurs. Exceeding the critical threshold for the onset of the VLF mode, these disturbances prevail the axial phase diffusion. Following this we stated that these phase differences are most likely the driving forces for the VLF mode [15].

In the present paper we concentrated on a restricted wavelength range but a variable aspect-ratio range. It was found that, increasing the Reynolds number, for $\lambda < 1.78d$ one observes—independently of the number of vortices of the flow system—always the same sequence of states. This is, first, the transition from Taylor vortex flow (TVF) to the onset of the small-jet mode via a Hopf bifurcation going along with a simultaneous breaking of the axial symmetry of the flow; second, the onset of the VLF mode via a homoclinic bifurcation for smaller cylinders where the underlying WVF is still the small-jet mode (therefore we have a T^2 torus); and finally, the transitions to chaos, which were found to be period-doubling routes on T^2 tori.

A model of interacting time-dependent Taylor vortex flow has been proposed by L’vov, Predtechensky, and Chernykh [30–32,60]. According to their experiments for $\eta=0.63$ and $\lambda \approx 2.0d$, the first unstable time-dependent mode is the oscillation of the outward boundaries [61]. The theory considers the oscillations of outward jets in each Taylor vortex pair as an independent nonlinear object obeying a simple Hopf bifurcation to a “fast” limit cycle. There is no more complexity in each vortex pair in this approximation [31,32,62]. The authors claim that this phenomenological model can be derived from the Navier-Stokes equations in much the same way as the Ginzburg-Landau equation [31]. This interaction produces a *global amplitude and phase modulation of all the interacting time-dependent vortices* going along with a breakdown of the azimuthal wave coherence of the time-dependent outflow jets. The effect can be observed as a splitting of the fundamental “fast” frequency in the velocity power spectrum and a slow modulation of the amplitudes (of the time-dependent outflow jets), with a corresponding low frequency peak in the velocity power spectrum arising with characteristic time scales of the order of the inverse line width $\Delta\omega_{\text{jet}}^{-1}$. Thus the authors refer to this effect as a “slow modulation” of the spatiotemporal envelopes of the oscillations of the underlying outflow jets. From the theoretical point of view this slow modulation appears due to fundamental resonant relations between the nonlinear modes.

There are several analogies between the model of interacting time-dependent Taylor vortex flow, assuming a weak interaction between the adjacent time-dependent vortices, the

experimental observations of the slow modulation reported in [31,32], and the VLF mode presented here. Only some are pointed out here: First, the transition from Taylor vortex flow to time-periodic Taylor vortex flow in our experiment takes place as the onset of the small-jet mode via a Hopf bifurcation, satisfying the main assumption of the model, that the first unstable time-dependent mode is the oscillation of the outward boundaries. Second, the onset of the “slow modulation” [31,32] as well as the onset of the VLF mode can be observed as a splitting of the fundamental “fast” frequency of the small-jet mode in the velocity power spectrum and a slow modulation of its amplitude going along with the appearance of a corresponding low frequency peak in the velocity power spectrum and exhibiting similar characteristic time scales (compare Fig. 3 in [31] or Fig. 12.3 in [32] and Fig. 3 in this paper). Third, the onset of the global phase modulation in [31,32], as well as the onset of the VLF mode [15], is caused by a breakdown of the azimuthal wave coherence of the underlying instability of the outflow jet.

To conclude, we have presented experimental investigations of the VLF mode in Taylor-Couette flow covering the whole wavelength and a wide aspect-ratio range up to flow systems having 50 vortices. We have proposed a mechanism for the onset of this mode and have found that—in a wavelength range $\lambda < 1.78d$ —the flow always shows the same transition to weak turbulence, i.e., via period-doubling-on-a-torus. A comparison with investigation by L’vov and co-

workers has shown that the VLF mode may appear also in a wide radius-ratio range. In a model proposed by these authors, a slow modulation of the underlying oscillations of the different outflow jets which can be identified with the VLF mode, also appears as a secondary time-dependent instability covering the whole parameter range.

We have shown that the interaction of different stationary and time-dependent modes appearing in the flow system which can be prepared definable and investigated carefully in a high-precision experiment can help to give a basis for the understanding of pattern formation and transition to weak turbulence in Taylor-Couette flow. Following our argument the appearance of the VLF mode displays a universal property for Taylor-Couette flow.

ACKNOWLEDGMENTS

We thank Tom Mullin for reading the manuscript carefully and many productive discussions, Alexei Predtechensky for the translation of Ref. [60] and for a helpful introduction to and a fruitful discussion about the “theory of interacting time-dependent Taylor vortex flow.” We thank Axel Sommerfeldt who performed some of the measurements shown in Figs. 13, 15, and 16 and writing the program for the data recording. Finally we gratefully acknowledge the financial support by the Deutsche Forschungsgemeinschaft under Grant No. DFG Pf210/3-2 and Pf210/3-3.

-
- [1] G. I. Taylor, *Philos. Trans. R. Soc. London, Ser. A* **233**, 289 (1923).
- [2] T. B. Benjamin, *Proc. R. Soc. London A* **359**, 1 (1978).
- [3] T. Mullin, *IMA J. Appl. Math.* **46**, 19 (1991).
- [4] T. Mullin, *The Nature of Chaos* (Oxford University Press, Oxford, 1993).
- [5] M. Golubitsky and I. Stewart, *SIAM J. Math. Anal.* **17**, 249 (1986).
- [6] D. Ruelle, *Arch. Ration. Mech. Anal.* **51**, 136 (1973).
- [7] D. Coles, *J. Fluid Mech.* **21**, 385 (1965).
- [8] G. P. King and H. L. Swinney, *Phys. Rev. A* **27**, 1240 (1983).
- [9] G. P. King, PhD thesis, University of Texas at Austin, 1983 (unpublished); and (unpublished).
- [10] G. Pfister, A. Lorenzen, and T. Mullin, *Phys. Fluids* **26**, 10 (1983).
- [11] G. Pfister and U. Gerdts, *Phys. Lett. A* **83**, 23 (1981).
- [12] K. Park, *Phys. Rev. A* **29**, 3458 (1984).
- [13] T. Mullin and T. B. Benjamin, *Nature* **288**, 567 (1980).
- [14] T. Mullin, *Phys. Rev. A* **31**, 1216 (1985).
- [15] U. Gerdts, J. von Stamm, Th. Buzug, and G. Pfister, *Phys. Rev. E* **49**, 4019 (1994).
- [16] A. Davey, R. C. DiPrima, and J. T. Stuart, *J. Fluid Mech.* **31**, 17 (1968).
- [17] C. A. Jones, *J. Fluid Mech.* **102**, 249 (1981); **157**, 135 (1985).
- [18] P. S. Marcus, *J. Fluid Mech.* **146**, 45 (1984); **146**, 65 (1984).
- [19] W. S. Edwards, S. R. Beane, and S. Varma, *Phys. Fluids A* **3**, 1510 (1991).
- [20] R. C. DiPrima, P. M. Eagles, and B. S. Ng, *Phys. Fluids* **27**, 2403 (1984).
- [21] K. T. Coughlin and P. S. Marcus, *J. Fluid Mech.* **234**, 1 (1992); **234**, 19 (1992).
- [22] M. Gorman and H. L. Swinney, *J. Fluid Mech.* **117**, 123 (1982).
- [23] L.-H. Zhang and H. L. Swinney, *Phys. Rev. A* **31**, 1006 (1985).
- [24] A. Brandstätter, J. Swift, H. L. Swinney, A. Wolf, J. D. Farmer, E. Jen, and P. J. Crutchfield, *Phys. Rev. Lett.* **51**, 1442 (1983).
- [25] A. Brandstätter and H. L. Swinney, *Phys. Rev. A* **35**, 2207 (1987).
- [26] T. Mullin, K. A. Cliffe, and G. Pfister, *Phys. Rev. Lett.* **58**, 2212 (1987).
- [27] K. T. Coughlin, PhD thesis, Harvard University, 1990 (unpublished).
- [28] D. Walgraef, P. Brockmans, and G. Dewel, *Phys. Rev. A* **29**, 1514 (1984).
- [29] H. Fasel and O. Booz, *J. Fluid Mech.* **138**, 21 (1984).
- [30] V. S. L’vov and A. A. Predtechensky, Institute of Automation and Electrometry, No. 111 (Novosibirsk, 1979).
- [31] V. S. L’vov, A. A. Predtechensky, and A. I. Chernykh, *Sov. Phys. JETP* **53**, 562 (1981).
- [32] V. S. L’vov, A. A. Predtechensky, and A. I. Chernykh, in *Nonlinear Dynamics and Turbulence*, edited by G. I. Barenblatt, G. Iooss, and D. D. Joseph (Pitman, Boston, 1983), p. 238.
- [33] G. Pfister, U. Gerdts, A. Lorenzen, and K. Schätzel, in *Photon Correlation Techniques in Fluid Mechanics*, edited by O. Schulz-Dubois, Springer Series in Optical Science Vol. 38 (Springer, New York, 1983), p. 256.
- [34] G. Pfister, U. Gerdts, F. Schulz, and G. Geister (unpublished).

- A summary of this paper is given in K. Bühler, J. E. R. Coney, M. Wimmer, and J. Zierep, *Acta Mech.* **62**, 47 (1986).
- [35] T. Mullin and K. A. Cliffe, in *Nonlinear phenomena and chaos*, edited by S. Sarkov (Adam Hilger, Bristol; 1986).
- [36] G. Pfister, H. Schmidt, K. A. Cliffe, and T. Mullin, *J. Fluid Mech.* **191**, 1 (1988).
- [37] J. von Stamm, Th. Buzug, and G. Pfister, *Phys. Lett. A* **194**, 173 (1994).
- [38] G. P. King, Y. Li, W. Lee, H. L. Swinney, and P. S. Marcus, *J. Fluid Mech.* **141**, 365 (1984).
- [39] P. Glendinning and C. Sparrow, *J. Stat. Phys.* **35**, 645 (1983).
- [40] T. Mullin and T. J. Price, *Nature* **340**, 294 (1989).
- [41] H. A. Snyder, *J. Fluid Mech.* **35**, 273 (1969).
- [42] M. Basset and J. Hudson, *Physica D* **35**, 289 (1989).
- [43] K. McKell, D. Broomhead, R. Jones, and D. Hurle, *Europhys. Lett.* **12**, 513 (1990).
- [44] A. C. Skeldon and T. Mullin, *Phys. Lett. A* **166**, 224 (1992).
- [45] J.-M. Flesselles, V. Croquette, and S. Jucquois, *Phys. Rev. Lett.* **72**, 2871 (1994).
- [46] H. Haucke, Y. Maeno, and J. Wheatly, in *LT-17, Proceedings of the 17th International Conference on Low Temperature Physics*, edited by U. Eckern, A. Schmid, W. Weber, and H. Wühl (Elsevier, Karlsruhe, 1984), pp. 1123–1124.
- [47] V. Franceschini, *Physica D* **6**, 285 (1983).
- [48] K. Kaneko, *Prog. Theor. Phys.* **69**, 1806 (1983).
- [49] A. Arnéod, P. H. Coullet, and E. A. Spiegel, *Phys. Lett. A* **94**, 1 (1983).
- [50] G. Pfister, in *Laser Anemometry in Fluid Mechanics*, edited by D. F. G. Durao (Ladoan, Portugal, 1984), p. 159.
- [51] H. Horner, *Phys. Rev. A* **27**, 1270 (1983).
- [52] Th. Buzug, J. von Stamm, and G. Pfister, *Physica A* **191**, 559 (1992).
- [53] Th. Buzug, J. von Stamm, and G. Pfister, *Phys. Rev. E* **47**, 1054 (1993).
- [54] F. Takens, in *Dynamical Systems and Turbulence*, edited by D. A. Rand and L.-S. Young, *Lecture Notes in Mathematics* Vol. 898 (Springer, Berlin, 1980), p. 230.
- [55] Th. Buzug, T. Reimers, and G. Pfister, *Europhys. Lett.* **13**, 605 (1990).
- [56] Th. Buzug and G. Pfister, *Phys. Rev. A* **45**, 7073 (1992).
- [57] Th. Buzug, *Analyse chaotischer Systeme* (BI-Wissenschaftsverlag, Mannheim, 1994).
- [58] Th. Buzug and G. Pfister, *Physica D* **58**, 127 (1992).
- [59] P. Grassberger and I. Procaccia, *Physica D* **9**, 189 (1983).
- [60] A. I. Chernykh, Institute of Automation and Electrometry, No. 147 (Novosibirsk, 1981) (in Russian).
- [61] A. A. Predtechensky (personal communication).
- [62] S. N. Lukaschuk, V. S. L'vov, A. A. Predtechensky, and A. I. Chernykh, in *Laminar-Turbulent Transition, IUTAM Symposium Novosibirsk 1984*, edited by V. V. Kozlov (Springer, Berlin, 1985), p. 653.